

Mapping of functional SARS-CoV-2 receptors in human lungs establishes differences in variant binding and SLC1A5 as a viral entry modulator of hACE2



Annarita Miluzio,^a Alessandro Cuomo,^b Chiara Cordiglieri,^a Lorena Donnici,^a Elisa Pesce,^a Mauro Bombaci,^a Matteo Conti,^a Alessandra Fasciani,^a Luigi Terracciano,^c Lara Manganaro,^a Mirco Toccafondi,^a Alessandra Scagliola,^a Stefania Oliveto,^a Sara Ricciardi,^{a,f} Renata Grifantini,^a Raffaele De Francesco,^{a,d} Sergio Abrignani,^{a,e} Nicola Manfrini,^{a,f,*} and Stefano Biffo^{a,f,**}



^aNational Institute of Molecular Genetics, "Fondazione Romeo ed Enrica Invernizzi", INGM, 20122, Milan, Italy

^bDepartment of Experimental Oncology, IEO, European Institute of Oncology IRCCS, 20141, Milan, Italy

^cInstitute of Pathology, University Hospital Basel, 4031, Basel, Switzerland

^dDepartment of Pharmacological and Biomolecular Sciences, University of Milan, 20133, Milan, Italy

^eDepartment of Clinical Sciences and Community Health, University of Milan, 20122, Milan, Italy

^fDepartment of Biosciences, University of Milan, 20133, Milan, Italy

Summary

Background The COVID-19 pandemic is an infectious disease caused by SARS-CoV-2. The first step of SARS-CoV-2 infection is the recognition of angiotensin-converting enzyme 2 (ACE2) receptors by the receptor-binding domain (RBD) of the viral Spike (S) glycoprotein. Although the molecular and structural bases of the SARS-CoV-2-RBD/hACE2 interaction have been thoroughly investigated *in vitro*, the relationship between hACE2 expression and *in vivo* infection is less understood.

Methods Here, we developed an efficient SARS-CoV-2-RBD binding assay suitable for super resolution microscopy and simultaneous hACE2 immunodetection and mapped the correlation between hACE2 receptor abundance and SARS-CoV-2-RBD binding, both *in vitro* and in human lung biopsies. Next, we explored the specific proteome of SARS-CoV-2-RBD/hACE2 through a comparative mass spectrometry approach.

Findings We found that only a minority of hACE2 positive spots are actually SARS-CoV-2-RBD binding sites, and that the relationship between SARS-CoV-2-RBD binding and hACE2 presence is variable, suggesting the existence of additional factors. Indeed, we found several interactors that are involved in receptor localization and viral entry and characterized one of them: SLC1A5, an amino acid transporter. High-resolution receptor-binding studies showed that co-expression of membrane-bound SLC1A5 with hACE2 predicted SARS-CoV-2 binding and entry better than hACE2 expression alone. SLC1A5 depletion reduces SARS-CoV-2 binding and entry. Notably, the Omicron variant is more efficient in binding hACE2 sites, but equally sensitive to SLC1A5 downregulation.

Interpretation We propose a method for mapping functional SARS-CoV-2 receptors *in vivo*. We confirm the existence of hACE2 co-factors that may contribute to differential sensitivity of cells to infection.

Funding This work was supported by an unrestricted grant from "Fondazione Romeo ed Enrica Invernizzi" to Stefano Biffo and by AIRC under MFAG 2021 - ID. 26178 project – P.I. Manfrini Nicola.

Copyright © 2022 The Authors. Published by Elsevier B.V. This is an open access article under the CC BY-NC-ND license (<http://creativecommons.org/licenses/by-nc-nd/4.0/>).

Keywords: Spike; Super resolution microscopy; ACE2 co-factors; RBD; Viral binding; Viral entry

eBioMedicine

2023;87: 104390

Published Online XXX

<https://doi.org/10.1016/j.ebiom.2022.104390>

1016/j.ebiom.2022.104390

Abbreviations: ACE2, Angiotensin-Converting Enzyme 2; RBD, Receptor-Binding Domain; S, Spike

*Corresponding author. National Institute of Molecular Genetics, "Fondazione Romeo ed Enrica Invernizzi", INGM, 20122, Milan, Italy.

**Corresponding author. National Institute of Molecular Genetics, "Fondazione Romeo ed Enrica Invernizzi", INGM, 20122, Milan, Italy.

E-mail addresses: manfrini@ingm.org (N. Manfrini), biffo@ingm.org (S. Biffo).

Research in context

Evidence before this study

Human Angiotensin-Converting Enzyme 2 (hACE2) is the receptor for Severe Acute Respiratory Syndrome Coronavirus-2 (SARS-CoV-2). To date, mapping of available and functional receptors is inferred by hACE2 immunohistochemical staining and relies on the assumption that all hACE2 molecules are capable to bind SARS-CoV-2 with equal efficiency. Consequently, hACE2 expression level is considered a prognostic marker that correlates with SARS-CoV-2 infection. Although easy and direct, one major limit of this approach is that it does not take into account the existence of other players which may promote or impair viral particle binding, or the possibility that not all hACE2 receptors are competent for interaction with SARS-CoV-2. Hence, a more efficient assay is required for specifically determining only those SARS-CoV-2 receptors that are functionally competent for viral binding.

Added value of this study

By using the Receptor Binding Domain (RBD) of the viral Spike (S) protein, we developed a binding assay for direct detection of SARS-CoV-2 competent receptors. Through mapping of functional viral binding sites both *in vitro* and *ex situ*, we show that only part of hACE2 receptors are actually competent for SARS-CoV-2 interaction. Our results suggest the presence of auxiliary, yet unknown, cofactors that modulate efficient viral binding. With this approach, we identified SLC1A5 as a modulating factor of SARS-CoV-2 binding in human lungs whose downregulation reduces the entry of SARS-CoV-2 variants.

Implications of all the available evidence

The approach described in this study allows a better comprehension of SARS-CoV-2 individual and organ-specific susceptibility to infection. The technology can be applied to establish new targets for co-receptor inhibition/modulation.

Introduction

The COVID-19 pandemic, caused by the SARS-CoV-2 betacoronavirus, emerged in late 2019 in Wuhan, China. Since then, the pandemic has swept across the world resulting in serious morbidity and mortality, deeply affecting economies. In order to restrain the spreading of the pandemic and limit the burden of intensive care units, social distancing measures have been applied throughout the world. Several approved vaccines against SARS-CoV-2 and many others in phase III clinical trial¹ are effective in reducing the disease burden. However, well-established treatments for SARS-CoV-2 infection of the critically ill are still under investigation.² In addition, the appearance of COVID-19 long-hauler syndrome³ raises questions on which types of cells are infected by the virus.

SARS-CoV-2 shares molecular similarities with SARS-CoV-1. The SARS-CoV-2 Spike (S) glycoprotein contains a receptor-binding domain (RBD) that recognizes angiotensin-converting enzyme 2 (ACE2) as its receptor. The importance of hACE2 expression in SARS-CoV-2 infection is demonstrated by the fact that engineered hACE2 receptor traps neutralize SARS-CoV-2.⁴ hACE2 is expressed as a membrane-bound protein in several human tissues such as lung, intestine, heart and kidney. Its surface expression was demonstrated on ciliated bronchial cells and on lung alveolar epithelial cells,⁵ which are a major pathological target of viral SARS-CoV-2 infection. However, hACE2 is also expressed in endothelial cells, increasing the potential risk of vasculitis and of virus spreading in other organs.^{6–11} Finally, the presence of SARS-CoV-2 entry sites in human glossopharyngeal and vagal nerves bears clinical implications for neuronal involvement.¹² In

agreement with the role of hACE2 in virus uptake by cells, up-regulation of human hACE2 causes increased disease severity in mice.¹³ Based on these studies, the level of expression of hACE2 is an important factor in predicting the SARS-CoV-2 infection. The emergence of new variants that have different cellular tropism, suggests that co-factors other than ACE2 itself may modulate cellular infectivity.¹⁴

It is normally assumed that hACE2 expression, detected through antibody binding, may reflect the number of cells susceptible to viral infection. In this study, we compared the number of SARS-CoV-2-RBD binding sites to that of hACE2 receptors and evaluated whether unidentified co-factors may account for viral infection. We developed a new *in vivo* binding method and concluded that additional hACE2 cofactors are important for efficient viral binding. Notably, different SARS-CoV-2-RBD variants differ in their capability to bind hACE2 positive cells.

Methods

Cell lines and culturing

All the cell lines used in this study except the HEK293TN cell line, were purchased from the American Type Culture Collection (ATCC).

The hACE2-HEK293TN cell line was produced by engineering the HEK293TN cell line (System Bioscience, cat. No. LV900A-1) through lentiviral transduction in order to stably express the hACE2 receptor.¹⁵ The lentiviral vector used was produced using transfer vector pLENTL_hACE2_HygR (see the “[plasmids](#)” section for details) following a standard procedure based on calcium phosphate cotransfection with 3rd generation

helper plasmids as described in the “[Lentivirus preparation](#)” section.

The hACE2 lentiviral vector obtained was used to transduce HEK293TN cells. 48 h after transduction cells were subjected to antibiotic selection with 250 µg/ml hygromycin. Expression of hACE2 in transduced cells was confirmed by flow cytometry staining using Anti-hACE2 primary antibodies (R&D systems, cat. No. AF933) (0.75 µg/200.000 cells) and rabbit anti-goat IgG (Alexa Fluor 647, Thermofisher Scientific cat. No. A21446) secondary antibodies (1:200 in PBS + 2% FBS). The expression of hACE2 was observed in more than 90% of the cells and was stable after several passages.

HEK293T, HEK293TN, hACE2-HEK293TN, Vero, Calu-3 and Huh-7.5 cells were cultured in DMEM medium supplemented with 10% FBS, 100 U/ml penicillin, 100 µg/ml streptomycin and 1% glutamine.

For HEK293TN-hACE2 cells, 250 µg/ml Hygromycin were also added to the medium in order to maintain plasmid selection.

Human samples

Immunofluorescence studies were performed on normal tissue samples of human lung biopsies derived from six randomly selected patients, as described in the main text. In detail, for each patient, we analyzed normal tissues adjacent to the tumoral or pathological site. The criteria for inclusion was the presence of sufficient normal tissue for the analysis to be performed, and high quality morphological samples.

Ethics. Informed consent was obtained from each patient and the study protocol was approved by the Ethical Committee of the Institute of Pathology, University Hospital Basel, Switzerland. Protocol number EKNZ 2020-00780.

Plasmids

The human codon-optimized nucleotide sequence encoding the RBD domain of the SARS-CoV-2 S glycoprotein (residues 318–541) derived from an early SARS-CoV-2 sequence isolate (GenBank MN908947-Wuhan-Hu-1) was subcloned into the mammalian expression vector pcDNA 3.4 (Genscript) generating the pcDNA 3.4 RBD_Cov2 expression vector.

The transfer vector pLENTI_hACE2_HygR was obtained by cloning the hACE2 ORF derived from the pcDNA3.1-hACE2 plasmid (Addgene cat. No. 145033) into the pLenti-CMV-GFP-Hygro vector (Addgene cat. No. 17446). hACE2 was amplified by PCR and inserted under the CMV promoter of the pLenti-CMV-GFP-Hygro, after GFP excision with XbaI and SalI digestion, thus generating the pLENTI_hACE2_HygR, which is now available to the scientific community through Addgene (Addgene cat. No. 155296).

The pcDNA3.1_spike_del19 plasmid was generated from the pcDNA3.1-SARS2-Spike plasmid (Addgene cat. No. 145032) by removing the last 19aa of the SARS-CoV-2-S coding sequence and is now available to the scientific community through Addgene (Addgene cat. No. 155297).

Lentiviral transfer plasmids encoding for shRNAs targeting SLC1A5 were purified from the following MISSION® shRNA glycerol stocks purchased from Sigma–Aldrich (SHCLNG-NM_009201): SLC1A5 Sh#1, TRCN0000043118; SLC1A5 Sh#2, TRCN0000043120; sh#3, TRCN0000288922.

Cloning, expression and purification of recombinant SARS-CoV-2-RBD

SARS-CoV-2-RBD and SARS-CoV-2-Spike-Omicron (B.1.1.529) were expressed through transient transfection of Expi293 cells (Expi293™ Expression System, Thermofisher Scientific) with the previously described pcDNA3.4 RBD_Cov2 plasmid and purified in a recombinant form which included an N-terminal signal peptide and the C-terminal octa-histidine-tag (GGHHHHHHHH). In brief, 50 µg of each protein-expressing plasmids were used to transfect approximately 7.5×10^6 cells/mL in 500 ml culture (95–99% cell viability), using the ExpiFectamine293 reagent under manufacturer’s recommendations and cultured for 3–4 days at 37 °C with a humidified atmosphere of 8% CO₂ on an orbital shaker at 125 rpm. The recombinant proteins were purified using Ni²⁺-NTA affinity chromatography by Akta-Pure (GE Life Sciences). Briefly, after clarification by centrifugation the supernatant was buffer exchanged with a binding buffer (Tris 20 mM, NaCl 10 mM, imidazole 10 mM pH = 8) using a HiPrep™ 26/10 desalting column. Then the proteins were: loaded onto a nickel-chelating resin pre-equilibrated with the binding buffer, washed with 10 column volumes of wash buffer containing 30 mM imidazole and eluted with the same buffer containing 300 mM imidazole at pH = 8. Peak fractions were analyzed by SDS-PAGE and fractions corresponding to the soluble SARS-CoV-2-RBD protein were pooled, buffer exchanged using a HiPrep™ 26/10 desalting column running in 1x PBS and stored at 4 °C.

To determine both SARS-CoV-2-RBD and SARS-CoV-2-Spike-Omicron recombinant protein purity, Size-Exclusion Chromatography with Right-Angle/Low-Angle Light Scattering (SEC–RALS/LALS) was performed using an OMNISEC system (Malvern Panalytical) coupled with a fluorescence detector RF-20 A (Shimadzu). Briefly, the two recombinant proteins were loaded on a Viscotek P2500 column 300 × 8 mm (Malvern Panalytical) with guard column PGuard 50 × 6 mm (Malvern Panalytical) and eluted with isocratic flow rate of 0.5 ml/min at 25 °C with phosphate-buffered saline as mobile phase.

Recombinant protein labelling

1.5 mg of either recombinant SARS-CoV-2-RBD or SARS-CoV-2-Spike-Omicron were labeled with Alexa Fluor 647™ (ThermoFisher Scientific cat. No. A20186). Same amounts of recombinant SARS-CoV-2-RBD were also labeled with Abberior STAR RED NHS bicarbonate (Abberior cat no. STRED-0002) fluorophore. Labeling with Alexa Fluor-647™ was performed following manufacturer's instructions. Briefly, 1 mg/ml of recombinant SARS-CoV-2-RBD in PBS was diluted in 1/10 of 1 M sodium bicarbonate solution. 100 µl of protein mix was added to the Alexa Fluor 647™ dye and incubated for 1 h at room temperature. The labeled protein was then purified on a chromatographic column in order to remove the unbound dye, and stored at 4 °C until use. Labeling with Abberior STAR RED was performed as follows. The Abberior STAR RED dye was diluted in DMSO 100% to a final concentration of 10 mg/ml. Recombinant SARS-CoV-2-RBD was incubated with the dye in a 1:2 M ratio for 1 h at room temperature with rotation. The labeled protein was then purified on a chromatographic column, as described above, and then stored at 4 °C until use.

Lentivirus preparation

293 T packaging cells were transiently transfected with calcium phosphate using the packaging plasmids pMD2.G/VSV-G (Addgene cat. No. 12259), pMDLg/pRRE (Addgene cat. No. 12251), pRSV-Rev (Addgene cat. No. 12253) and relevant transfer vectors. Twenty-four hours following transfection, the exhausted medium was removed and replaced. Virus-containing supernatants were collected 48 h after transfection, filtered with 0.45-µm pore-size filters and frozen at -80 °C until usage.

Lentiviral transduction for stable shSLC1A5 cell line generation

Viruses were produced as described in the “Lentivirus preparation” section using transfer vectors encoding for different SLC1A5 shRNAs (SLC1A5 sh#1, #2 and #3). For each 1×10^6 cells, 1.5 ml of crude viral supernatant was used for transduction with $4 \mu\text{g ml}^{-1}$ polybrene and spinoculated for 30' at 500 g. Cells were then incubated in 5% CO₂ at 37 °C for 12 h. Media were then replaced. After 24 h of viral infection, cells expressing puromycin resistance were selected with puromycin dihydrochloride (Sigma-Aldrich, cat. No. P7255) at $1 \mu\text{g ml}^{-1}$ until needed.

hACE2 transient transfection

HEK293T cells were grown in 15 cm dishes to 75% confluence in DMEM medium. Medium was replaced 4 h prior to transfection. Transfections were performed using the calcium phosphate method as previously described in¹⁶ with 32 µg of pCDNA3.1-hACE2 transfer vector

(Addgene cat. No. 145033), 125 mM CaCl₂ and HBS (140 mM NaCl, 50 mM HEPES, 0.75 mM Na₂HPO₄).

SARS-CoV-2-S pseudotyped lentiviral particle generation

SARS-CoV-2-S pseudotyped lentiviral particles were prepared as previously described.¹⁷ Briefly, 5×10^6 HEK-293TN cells were plated in 15-cm dish with complete DMEM medium. The following day, 32 µg of reporter plasmid pLenti CMV V5-LUC Blast (Addgene #21474), 12.5 µg of pMDLg/pRRE (Addgene #12251), 6.25 µg of pRSV-Rev (Addgene #12253), and 9 µg pCDNA3.1_spike_del19 were cotransfected following a standard procedure based on calcium phosphate transfection. After 12 h from transfection, the medium was removed and substituted with 16 ml of complete ISCOVE. 30 h after transfection, the supernatant was collected, clarified by filtration with a 0.45-µm pore-size filter and concentrated 400x by centrifugation for 2 h at 20,000 rpm using a SW32Ti rotor (Beckman Coulter). Viral pseudoparticles were aliquoted and stored at -80 °C until usage.

SARS-CoV-2 pseudoparticle infection, binding competition assays and pandemic SARS-CoV-2 virus infection

For SARS-CoV-2 pseudoparticles infection Vero or Huh7.5 were plated at 10^4 cells/well in white 96 well plates in complete DMEM medium. The day after, cells were infected adding 50 µl/well of SARS-CoV-2-S pseudotyped lentiviral particle-containing medium at increasing MOI.^{1,5,10}

In binding competition assays, 1 h prior to infection Vero cells were preincubated at 37 °C with increasing concentration of Anti-hACE2 Antibodies or recombinant SARS-CoV-2.

To evaluate V-9302 compound effect on pseudoparticle infection, Huh7.5 were pre-treated for 1 h at 37 °C with V-9302 and then infected at 1MOI for 3 h in presence of V-9302. After 3 h a PBS wash was performed and medium was changed. 48 h post-infection both cell viability and infection outcome were measured with the Bright-Glo™ Luciferase System (Promega cat. No. E2610) and the Cell Titer blue CellTiter-Blue® Cell Viability Assay (Promega cat. No. G8080), respectively, using an Infinite F200 plate reader (Tecan).

The SARS-CoV-2 D614G isolate (SARS-CoV-2/human/ITA/Milan-UNIMI-1/2020, GenBank MT748758.1, GISAID ref. seq. EPI_ISL_584051) was propagated in Vero cells. Briefly, 450,000 Vero cells were plated into 6 well plate in DMEM 2% FBS. 24 h later cells were inoculated with 0.01 MOI of the original SARS-CoV-2 viral stock (Professor Serena Delbue, UNIMI). SARS-CoV-2 was collected 48–72 h later, filtered through a PES 0.45 µm filter, aliquoted and stored at -80 °C.

Huh-7.5 cells expressing either the Sh-pLko or Sh#2-SLC1A5 vector, were plated in 48 multiwell plates. The subsequent day cells were infected with either the SARS-CoV-2 D614G virus or the Omicron 1 variant B.1.1.529 (GISAID ref. seq. EPI_ISL_10898045) at a MOI of 0.1. Prior to infection SARS-CoV-2 was pre-incubated with Anti-Spike antibody (10 µg/ml, Sino biologicals 4059_T62) as an entry inhibitor control for 30 min at 37 °C. Samples were collected 24 h post infection.

Calu-3 cells expressing either the Sh-pLko or Sh#2-SLC1A5 vector, were plated in 48 multiwell plates and two days after they were infected with SARS-CoV-2 D614G virus at a MOI = 0.1 for 2 h at 37 °C in complete medium with 2% FBS. After infection, virus wash out was performed and cells were maintained at 37 °C for 72 h. At 24 h post infection cells were collected for RNA extraction, RT-qPCR quantification of SARS-CoV-2 intracellular RNA and intracellular staining of SARS-CoV-2 protein, while 24 and 72 h post infection supernatants were collected for qPCR quantification of SARS-CoV-2 genome.

Cellular RNA was isolated using the RNeasy Kit (Qiagen), cDNA was obtained using the SuperScript@VILOTM cDNA synthesis kit (Thermo Fisher Scientific) and expression of SARS-CoV2 NP was determined by Taqman PCR (2019-nCoV RUO Integrated DNA Technologies). Data were normalized on RNaseP.

Supernatants were subjected to lysis with ViRNAex solution (Cabru) and SARS-CoV-2 genome was quantified by absolute qPCR (TaqPath™ 1-Step RT-qPCR Master Mix, CG, ThermoFisher Scientific) using a specific primer/probe (2019-nCoV RUO Integrated DNA Technologies) and standard to determined viral copy number (2019_nCoV_N Positive control, integrated DNA Technologies).

Intracellular staining of SARS-CoV-2 nucleoprotein was performed using fixation/permeabilization kit (BD bioscience) using Anti-SARS-CoV-1/2 NP Antibody (ZMS1075, Sigma Aldrich) and Goat anti-Mouse IgG, Alexa Fluor 488 (ThermoFisher Scientific) at 1:200 dilution. The percentage of infected cells was determined relative to not infected cells by flow cytometry analysis.

V-9302 treatment

Huh-7.5 cells were treated with either 15 or 20 µM V-9302 for 3 h (cell fractioning and flow cytometry experiments) or with increasing concentrations of V-9302 (Selleckchem, cat No. S8818) for 16 h (pseudoparticle experiments).

SARS-CoV-2-RBD binding ELISA

Huh-7.5 cell monolayers, were cultured in the 96-well plate for 24 h at a final confluence of 70–80%. For SLC1A5 shRNA experiments cell were left untreated, while for V-9302 experiments cells were treated for 3 h with 25 µM V-9302. After washing with PBS the cells were

incubated with either 10 µg/ml (for shRNA experiments) or 5 µg/ml (for V-9302 experiments) of biotinylated recombinant SARS-CoV-2-RBD for 1 h at RT. The plate was washed again with PBS and 100 µl of diluted streptavidin HRP-conjugate were added to each well. The plate was incubated at room temperature for 1 h. The wells were then washed and 100 µl of solution containing TMB was added and incubated at RT in the dark for 5–10 min. The plate was monitored until a blue color was visible, indicating that a correct reaction occurred. The reaction was stopped by adding 100 µl of stop solution to each well. The absorbance was recorded at 450 nm within 10 min on an Infinite F200 Multimode Microplate Reader (Thermo Fischer Scientific, USA).

FACS analysis for detection of membrane-bound hACE2, for quantifying SARS-CoV-2-RBD and SLC1A5 and SARS-CoV-2-Spike-Omicron binding

5×10^5 HEK 293 T cells transiently expressing hACE2, 5×10^5 Vero cells, or 5×10^5 Huh-7.5 cells, were pelleted, washed once in PBS, re-suspended in 100 µl PBS and stained with:

1) 2 µl of anti-hACE2 antibodies (R&D systems, cat. No. AF933) for 30' at 37 °C followed by incubation with anti-goat Alexa Fluor 488™ secondary antibodies (ThermoFisher Scientific, cat. No. A-11078) for additional 30' at 37 °C; 2) 1,5 or 3 µg of Alexa-Fluor-488-labeled-SARS-CoV-2-RBD for 30' at 37 °C. Stained cells were then washed twice in PBS, harvested and analysed on a BD FACSCanto II machine. All subsequent analyses were performed using FlowJo. For stripping experiments, 5×10^5 HEK cells transiently expressing hACE2 and stained with 3 µg of recombinant SARS-CoV-2-RBD, were either left untreated or treated for 30'' with stripping buffer (0.2 M acetic acid, 0.5 M NaCl in PBS) in order to remove any protein binding to surface receptors. After washing in PBS, cells were harvested and analyzed as described.

For detection of SLC1A5, 5×10^5 Huh-7.5 cells, either left untreated or treated with V-9302 as described in 2.11, were fixed with 2% formaldehyde, stained with 2 µl of anti-SLC1A5 antibodies (Cell Signaling Technology, cat. No. 5345 and 8057) for 30' at 37 °C and incubated with anti-rabbit Alexa Fluor 488™ secondary antibodies (ThermoFisher Scientific, cat. No. A-11010) for additional 30' at 37 °C.

For SARS-CoV-2-Spike-Omicron binding experiments, 5×10^5 HEK 293 T cells constitutively expressing hACE2 were stained as in 2) but using 3 µg of Alexa-Fluor-647-labeled SARS-CoV-2-Spike-Omicron (B.1.1.529).

Isolation of cytoplasmic and membrane proteins fractions

Experiments were performed in Huh-7.5 cells either treated with 15 µM of V-9302 compound for 3 h or left untreated (NT) and in Huh-7.5 cells downmodulated for SLC1A5.

Cells were centrifuged at 1200 rpm and pellets were lysed with 300 µl ice cold PBS containing protease inhibitors (Sigma Aldrich, cat. No. P8340). The lysates were frozen at -80°C for 1 h and thawed at RT. After three freeze–thaw cycles, samples were centrifuged at 13000 g for 30 min at 4°C and the supernatants were harvested for the cytosolic protein fraction. The pellets were then resuspended with 150 µl of membrane protein isolation buffer (150 mM NaCl, 20 mM Tris–HCl pH 7.5, 1 mM EDTA, 1 mM EGTA and 1% Triton X-100) containing protease inhibitors (Sigma Aldrich, cat. No. P8340). The lysates were sonicated on ice for three cycles of 10" ON/10" OFF and then centrifuged at 13000 g for 30 min at 4°C . The supernatants were harvested for solubilized membrane protein fractions. Total protein extracts were obtained from combining both cytosolic and membrane protein fractions. hACE2 and GAPDH antibodies were used as membrane and cytoplasmic controls, respectively.

Western blotting

Western blots were performed as described in¹⁸. Briefly, cell samples were lysed in RIPA buffer and protein lysates were loaded on polyacrylamide gels. Western blots were performed using the following antibodies: anti-hACE2 (R&D systems, cat. no. AF933); anti-SARS-CoV-2-RBD (Sino Biological, cat. No. 40592-T62); anti-SLC1A5 (Cell Signaling Technology, cat. No. 5345 and 8057); anti-β-Actin (Sigma–Aldrich, cat. no. A5441) and anti-GAPDH (Cell Signaling Technology, cat. No. 2118).

RNA extraction and RT-qPCR

RNA was extracted as described in¹⁹. Briefly, total RNA was purified from at least 10^6 cells using the TRIzol reagent (Thermo Fisher Scientific, cat. No. 15596026) and the RNeasy Mini Kit (Qiagen, cat. No. 74106) following manufacturers' instructions. 500 ng of RNA were reverse-transcribed using random primers and the SuperScriptIII First-Strand Synthesis SuperMix for qRT-PCR (Thermo Fisher Scientific, cat. No. 11752050). The synthesized cDNA was then analysed by RT-qPCR using the GoTaq qPCR Master Mix (Promega; cat. No. A6001) or TaqMan™ Universal PCR Master Mix, no AmpErase™ UNG (Thermo Fisher Scientific cat. No. 4324018). The following primers were used: *SLC1A5* FWD: 5'-CAT CAT CCT CGA AGC AGT CA-3'; *SLC1A5* REV: 5'-CTC CGT ACG GTC CAC GTA AT-3'; *18S* FWD: 5'-CAA CAC CAA CAT CGA TGG GC-3'; *18S* REV: 5'-TCA CAC GTT CCA CCT CAT CC-3'.

Co-immunoprecipitations

Co-immunoprecipitation of hACE2 from hACE2-HEK cells with or without SARS-CoV-2-RBD binding for mass spectrometry

HEK293TN and hACE2-HEK 293 TN cells were grown at 90% confluency in 150 mm plates. Cells were then

detached in PBS. After 3 washes, cells were resuspended in PBS buffer containing 20 µg/ml of recombinant SARS-CoV-2-RBD and incubated with agitation at 4°C for 60'. Primary amine crosslinker Disuccinimidyl Suberate (DSS) (Thermo Fisher Scientific cat. no. 21555) was then added to the mix at a 2 mM final concentration. Crosslinking reactions were performed at room temperature (RT) for 30 min in agitation and were then quenched by addition of 20 mM of TRIS pH 7.4 for 15'.²⁰ After two additional washes in PBS, cells were lysed in the following buffer: 50 mM TRIS pH 7.4, 150 mM NaCl, 1% TRITON and 1:100 protein inhibitor cocktail (Sigma–Aldrich cat. no. P8340).

1 mg of total cell lysates were then incubated for 2 h at 4°C in constant rotation with protein G Dynabeads (Life technologies cat. No. 10004D) previously incubated with 25 µg/ml of anti-hACE2 antibodies (R&D systems, cat. no. AF933). The beads were then washed three times with lysis buffer and proteins were eluted from the beads by incubation at 95°C for 10 min with 2X Laemmli sample buffer. Immunoprecipitated samples were then loaded on separate gels for silver staining (to control Immunoprecipitation efficiency), coomassie blue staining (for subsequent mass spectrometry analysis) and western blotting.

Co-immunoprecipitation of SLC1A5 from hACE2-HEK cells with or without SARS-CoV-2-RBD binding

Same cells as above were treated as described in the previous section except that co-immunoprecipitation was performed using G Dynabeads (Life technologies cat. No. 10004D) previously bound to anti-SLC1A5 antibodies (1:5 diluted) (Cell Signaling Technology, cat. No. 8057).

Mass spectrometry

hACE2 immunoprecipitated samples, prepared as described above, were loaded on polyacrylamide gels for coomassie blue staining. In brief, boiled samples were loaded on NuPAGE® Novex 4–12% gradient gels (Thermo Fisher Scientific, cat. no. NP0321PK2), and seven consecutive bands were excised and trypsin-digested following the procedure described by.²¹ In all cases, the protocol steps were the following: proprotein reduction in 10 mM DTT for 1 h at 56°C ; protein alkylation with 55 mM iodoacetamide for 45 min at room temperature in the dark and digestion with 12.5 ng/µl trypsin overnight at 37°C . Tryptic peptides were extracted from the gel with 3% trifluoroacetic acid (TFA) and 30% acetonitrile (ACN). The extracted peptides were cleaned up using homemade STAGE Tips microcolumns.²² Peptides were then eluted in 40 µl buffer B (80% ACN, 0.1% formic acid (FA)). ACN was evaporated using a speed vac concentrator (Eppendorf) and the volume of the eluates were adjusted to 5 µl with 1% TFA, to be then analysed by LC-MS/MS using an EASY-nLC 1200 (Thermo Fisher Scientific, cat.

No. LC140) connected to a Q-Exactive HF instrument (Thermo Fisher Scientific) through a nano-electrospray ion source (EASY-SPRAY, Thermo Fisher Scientific). The nano-LC system was operated in one column set-up with an EasySpray PEPMAP RSLC C18 column (Thermo Fisher Scientific) kept constant at 45 °C. Solvent A was 0.1% formic acid (FA) and solvent B was 0.1% FA in 80% ACN. Samples were injected in aqueous 1% (TFA) at a constant pressure of 980 Bar. Peptides were separated with a gradient of 3–35% solvent B over 49 min followed by a gradient of 30–60% for 5 min and 60–95% over 5 min at a flow rate of 300 nL/min. The Q-Exactive was operated in the data-dependent acquisition (DDA) to automatically switch between full scan MS and MSMS acquisition. MS spectra (from m/z 375–1650) were analysed in the Orbitrap detector with resolution $R = 70,000$ at m/z 400. The 12 most intense peptide ions with charge states ≥ 2 were sequentially isolated to a target value of $3e6$ and fragmented with a normalized collision energy setting of 28% in to the HCD cell. The maximum allowed ion accumulation times were 20 ms for full scans and 80 ms for MSMS. The dynamic exclusion time was set to 20 s. Acquired raw data were analysed for using the integrated MaxQuant version 1.6.2.3, using the Andromeda search engine.²³ False discovery rate (FDR) of all peptide identifications was set to a maximum of 1%. Carbamidomethylation of Cysteine was set as a fixed modification. The January 2021 version of the Uniprot Human sequence was used for peptide identification (77,027 Entries). The LFQ intensity calculation was enabled, as well as the *Match Between Runs* (MBRs) feature.²⁴ The “protein groups” output file from MaxQuant was analysed using Perseus software.²⁵ Briefly, no imputation was used, and the data were filtered to have 3 valid values in at least one group. Statistically significant enriched proteins were filtered using a threshold setting for differential analysis of $S0 = 0.1$ and $FDR = 0.05$ (see [Supplementary Table](#)).

Data-mining of mass spectrometry data

Proteins significantly enriched in the hACE2 + SARS-CoV-2-RBD co-immunoprecipitation (either with a p -value < 0.05 or with lack of detected peptides in each of the three MOCK controls) were crossed with all published SARS-CoV-2 interactors present in the BIOGRID database (https://thebiogrid.org/search.php?search=SARS-CoV-2*&organism=2697049) as of December 16, 2020. Each significantly enriched protein was given a score based on the total number of previously found interactions with SARS-CoV-2 proteins (1 point = 1 interaction). A $\times 4$ weighted score was given to each interaction with the Spike protein.

Immunofluorescence

Immunofluorescence was performed on cell lines or on frozen human lung sections, as previously described.¹⁶

Binding control

HEK293T, Vero and Huh-7.5 cell lines or human lung tissue sections (3 μm) were fixed with 3% PAF, subjected to a blocking step (goat serum plus 5%BSA) without permeabilization and later incubated with primary antibodies. Goat anti-hACE2 (R&D systems, cat No AF933) or rabbit anti-SLC1A5 (Cell Signaling, cat. No. 5345) primary antibodies were used overnight at 4 °C. Double staining controls were performed according to²⁶. 3 μg of recombinant SARS-CoV-2-RBD, SARS-CoV-2 Spike-Trimer (Miltenyi biotec, cat No 130-127-683) or SARS-CoV-2-Spike-Omicron (B.1.1.529) were labeled with either Molecular Probes AlexaFluor 647TM (ThermoFisher Scientific cat. No. A20186) or Abberior STAR RED NHS bicarbonate (Abberior cat no. STRED-0002) as described in the “[Recombinant protein labelling](#)” section. Recombinant proteins were added on cell lines and/or lung tissues for 1 h at RT. The following fluorescently-tagged secondary antibodies were incubated for 60' at room temperature to detect host species Igs of primary antibodies: anti-Goat-Alexa-Fluor 568, anti-rabbit-Alexa-Fluor 488, both diluted 1:500 (ThermoFisher Scientific, cat. No. A11057 and cat. No A11008 respectively) or Anti-Goat- Abberior-Star-ORANGE, Anti-Rabbit- Abberior-Star-ORANGE, anti-Rabbit Abberior-Star-RED, and anti-Goat-Abberior STAR520SXP (1:500, Abberior, cat. No. STO1055 and cat. No. STR1055, respectively). Alexa-Secondary antibodies were used for standard Laser-scanning Confocal microscopy and for video-confocal-super-resolution (VCS) structure illumination spinning disk microscopy, whereas Abberior-Secondary antibodies were employed for Super-resolution microscopy (STED) imaging. DAPI staining (Thermo-Fisher Scientific, cat. No D21490) was used to detect nuclei. Slides were mounted in ProLongTM Gold Antifade Mountant (ThermoFisher Scientific, cat. No. P10144) for conventional confocal microscopy and with ProLong Glass Mounting reagent (ThermoFisher Scientific, cat. No. P36984) for VCS and STED acquisitions. Images were acquired using either a laser-scanning confocal microscope (Leica Microsystems, model SP5 with 8 laser lines and 4 PMTs detectors), with excitation wavelengths of 488 nm, 568 nm, 647 nm for all different targets and 405 nm for DAPI nuclear labelling, or a Nikon-Crest multimodal automated microscope, equipped with X-lightV2-VCS spinning-disk/structure illumination head (CrestOptics) coupled with Andor-DU888 EM-CCD and Andor Zyla sCMOS cameras (Andor Technologies, Oxford Instruments, or a STED nanoscope (Abberior STEDYCON built on a Zeiss Axio Imager 2 upright automated widefield microscope with PIFOC nanopositioner and scanner) with a pulsed 775 nm STED laser and four excitation pulsed laser lines (404, 488, 561, 640). For the STED modality, excitation lasers were increased to 15–25% and the STED depletion laser was kept at 100% power on both emission channels to

achieve 40 nm resolution on the star-RED channel (SARS-CoV-2-RBD protein) and 57 nm resolution on the star-ORANGE channel (anti-hACE2), with $n = 7$ lines of accumulation and 20 nm pixel-size. For triple-channel STED, the third fluorochrome (STAR520SXP), a long Stoke's Shift dye, was excited with 35% power (at 488 nm) and depletion laser was kept at 65%, in order to obtain maximally 70 nm resolution. A 63x oil objective (NA 1.40, Leica microsystem), a 100x TIRF oil objective (NA 1.49, Nikon Instruments) and a 100x oil objective (NA 1.46, Zeiss) were used for confocal, VCS, and STED microscopy, respectively.

Binding competition

Immunofluorescence was performed on the same samples of the binding control experiments. Briefly, after fixation and blocking steps, all samples were pre-incubated with 9 μg of unlabeled SARS-CoV-2-RBD recombinant protein for 1 h at RT. After pre-incubation, all samples were exposed to primary antibodies directed against all the proteins of interest overnight at 4 °C. Subsequently, the unbound antibodies were removed and samples were incubated with 647-labeled-SARS-CoV-2-RBD recombinant protein for 1 h at RT. Bound primary antibodies were then detected by their specific fluorescently-tagged-secondary antibodies, as described above. Nuclei were stained with DAPI, and the images were acquired on a confocal microscope (Leica Microsystems, model SP5 with 8 laser lines and 4 PMTs detectors).

Binding control in living cells

Huh-7.5 cells were incubated with 3 μg of 647-labeled-SARS-CoV-2-RBD recombinant protein for 30 min at 37 °C, 5% CO₂. Without permeabilization, cells were fixed with 3% PAF and subjected to immunofluorescence staining: goat anti-hACE2 and rabbit anti-SLC1A5 primary antibodies were incubated overnight at 4 °C. Anti-goat-Alexa-Fluor568nm and anti-rabbit-Alexa-Fluor488nm secondary antibodies were added for 1 h at RT. Nuclei were stained with DAPI. Immunofluorescent images were acquired on a confocal microscope. All the images were further processed with the ImageJ software.

Live-cell time-lapse imaging

SARS-CoV-2-RBD live binding was determined on both HEK-MOCK and HEK-hACE2 expressing cells, via time-lapse spinning disk confocal microscopy using an environmentally-controlled (temperature and CO₂ sensors, OKO-Lab) Nikon-Crest multimodal automated microscope, equipped with X-lightV2-VCS spinning-disk/structure illumination head (CrestOptics) coupled with Andor-DU888 EM-CCD and Andor Zyla sCMOS cameras (Andor Technologies, Oxford Instruments) mounted on an inverted fully automated Ti microscope (Nikon Instruments), with multi-cores LED excitation

(SpectraAura, Lumencore and Pe-4000, CoolLed). Briefly, nuclei were stained with Hoechst 33,342 (ThermoFisher, cat. No. 62249) and images were acquired every 30 s on three different Fields of View for both HEK-MOCK and HEK-hACE2 cells. After the addition of 3 μg of 647-labeled SARS-CoV-2-RBD recombinant protein, live-imaging continued for additional 3 h. All acquisitions were performed on a Nikon-CREST XlightV2+Andor-Du888 microscope at 40x magnification. After live-imaging experiments, time-dependent frame-by-frame analyses of fluorescently-labeled-SARS-CoV-2-RBD signals were performed over time on both HEK-MOCK and HEK-hACE2 expressing cells. Cell surface SARS-CoV-2-RBD fluorescence intensity was also quantified: taking into consideration only 647-labeled-SARS-CoV-2-RBD positive cells, SARS-CoV-2-RBD fluorescence intensity was measured on both cell objects contours (for cell membrane measurements) and on object subtracted from cell contours (for intracellular compartment measurements), using digital imaging segmentation pipelines in NIS-Elements v.5.30 GA3 module (Lim-Instruments).

SARS-CoV-2-RBD-pHrodo Green live imaging was performed on HEK-hACE2 expressing cells, using a custom-implemented spinning-disk inverted microscope (Nikon/Crest) with a 40x (NA 0.95) air objective (Nikon) and LED excitation (Cool-LED) and a High-resolution Andor-Zyla sCMOS videocamera. Briefly, SARS-CoV-2-RBD Recombinant protein was labeled with pHrodo™ iFL Green Microscale Protein Labeling Kit (Invitrogen, cat No P36015), according to the manufacturer's protocol. Human Recombinant Epidermal Growth Factor (EGF)-pHrodo™ Green (Molecular Probes, Life Technologies, cat No P35375) was used as a positive control either alone or in combination with 647-labeled-SARS-CoV-2-RBD-Recombinant protein. pHrodo-labeled recombinant proteins were added on HEK-hACE2-expressing cells and maintained at 37 °C 5%CO₂ for 30 min, according to the manufacturer's instructions. After incubation, 647-labeled-SARS-CoV-2-RBD-Recombinant protein was added only in combination with EGF, as control. Live-cell time-lapse imaging recording was performed over 5 h with 6 min time-lapse for each considered condition. Finally, fluorescence signal intensity of all considered dyes was analyzed with an ad hoc created macro of commands in Fiji (ImageJ).

Imaging processing and analysis

Images from both confocal and STED microscopy were processed and analyzed via NIS-Elements V.5.30 software (Lim-Instruments). Confocal images from both cell and tissue samples were acquired at high resolution using a 63x oil objective plus further zooming-in magnification up to 3x or 6x for better intracellular structure appreciation. When needed, further image deconvolution was applied to improve image resolution, using 2D and 3D Richardson-Lucy algorithms within

the NIS-Elements deconvolution module. 3D reconstruction and visualization were conducted using the NIS-Element 3D-viewer module. Both time-lapse chosen video recordings and 3D rendering movies were saved at 10 fps reproduction rate. Ad-hoc designed pipelines of digital imaging analysis were implemented using the General Analysis 3 module of NIS-Elements, according to the assay necessities, i.e. both for quantification of SARS-CoV-2-RBD-, SARS-CoV-2-Spike-Trimer- and SARS-CoV-2-Spike-Omicron-binding within lung tissue samples and for colocalization studies. For image quantification, the thresholding signal was conducted using a machine learning pixel classification algorithm. Colocalization analyses were conducted on the best focal Z-plan among the Z-stack acquired for each field of view for best Pearson Index calculation. Double methodological analysis was conducted on all assays to check the colocalization values among studied signals, using both the Colocalization module within NIS-Elements V.5.30 and the Coloc-2 plugin in Fiji (<https://imagej.net/Coloc-2>). For best colocalization assessment, the measures were conducted both on whole-cell objects within cell samples and tissue samples, and within intracellular compartments with double (hACE2/SARS-CoV-2-RBD; hACE2/SLC1A5; SARS-CoV-2-RBD/SLC1A5) or triple (hACE2/SARS-CoV-2-RBD/SLC1A5) signals.

Statistics

Each experiment was repeated at least three times; means \pm SD or means \pm SEM between were calculated. Upon normal distribution, Student t-tests or ANOVA tests were used, otherwise, non-parametrical tests such as Mann-Whitney and Kruskal-Wallis tests were employed. Statistical P-values obtained as indicated: four asterisks **** for P-values less than 0.0001, three asterisks *** for P-values less than 0.001, two asterisks ** for P-values less than 0.01 and one asterisk * for P-values less than 0.05.

Role of funding source

The Funders of this study had no role in study design, data collection, data analysis or writing of the manuscript.

Results

hACE2 expression is not sufficient for pervasive SARS-CoV-2-RBD binding to human cells

Structural studies have demonstrated that the Receptor Binding Domain (RBD) of the Spike (S) protein of SARS-CoV-2 binds to the hACE2 receptor.²⁷ To investigate the correlation between hACE2 expression and viral binding to host cells, we designed an assay capable of quantifying functional hACE2 receptors, based on fluorescent SARS-CoV-2-RBD labeling. We constructed a codon-optimized SARS-CoV-2-RBD ORF (Fig. 1A), expressed it in eukaryotic cells and purified it to homogeneity from the supernatant (Fig. 1B, left and

center). By size-exclusion chromatography (SEC) coupled with static light scattering (SLS) analysis, we detected a unique eluted peak at a MW of 30.4 KDa, indicating the presence of a single monomeric protein (Fig. 1B, right). Next, pure monodispersed recombinant SARS-CoV-2-RBD was fluorescently-labeled. To assess its specificity, we tested its binding to the cell surface of either hACE2-expressing or MOCK control HEK293T cells (Fig. 1C). We confirmed that the presence of hACE2 was required for SARS-CoV-2-RBD binding, as the fluorescent signal was detectable only in hACE2-transfected cells (Fig. 1D). By co-Immunoprecipitation (co-IP) experiments, SARS-CoV-2-RBD was actually enriched only in hACE2 pulldowns of hACE2-expressing cells (Fig. 1E and Fig. S1A), confirming that SARS-CoV-2-RBD properly bound hACE2 expressing cells.

Next, we performed live-cell imaging to test the kinetics and extent of SARS-CoV-2-RBD binding to the surface of living HEK-hACE2 cells. SARS-CoV-2-RBD signals quickly reached the external side of HEK-hACE2 cells and accumulated on the plasma membrane compartment (Fig. 1F, Fig. S1B and Movies S1–S4). This result was confirmed by fluorescence quantitation, which revealed that SARS-CoV-2-RBD signals rapidly reached saturation (Fig. 1G). Next, we analyzed whether recombinant SARS-CoV-2-RBD could be internalized. To do so we labeled SARS-CoV-2-RBD with pHrodo™, a specific dye which becomes fluorescently detectable only when internalized in the acidic environment of phagosomes. We found that no discernible SARS-CoV-2-RBD intracellular signal could be detected. As a control, Epithelial Growth Factor (EGF), a protein known to be internalized upon receptor engagement, started to accumulate intracellularly after 2 h (Fig. S1C–S1E and Movies S5–S7). The confinement of SARS-CoV-2-RBD binding to the cell surface was further confirmed by flow cytometry, since removal of cell surface protein/protein interactions by acidic stripping completely abolished detection of any SARS-CoV-2-RBD signal (Fig. S2A). These results indicate that recombinant SARS-CoV-2-RBD binds to the cell surface, but is not internalized.

In order to define if the binding of SARS-CoV-2-RBD with hACE2 could faithfully reproduce the physiological binding between SARS-CoV-2 and hACE2, we checked whether the interaction could block the entry of SARS-CoV-2 pseudoparticles coated with the S protein. We used the Vero cell model²⁸ that expresses endogenous ACE2 levels (Fig. S2B and C) and first confirmed that it binds SARS-CoV-2-RBD (Fig. S2D); cells were viable throughout the procedure (Fig. S2E). Next, we generated viral particles pseudo-typed with SARS-CoV-2-S protein, and infected Vero cells in the presence of either unlabeled recombinant SARS-CoV-2-RBD or neutralizing anti-hACE2 antibodies (Fig. 1H). We found that viral entry was inhibited by increasing SARS-CoV-2-RBD concentrations (Fig. 1I), similarly to inhibition of viral

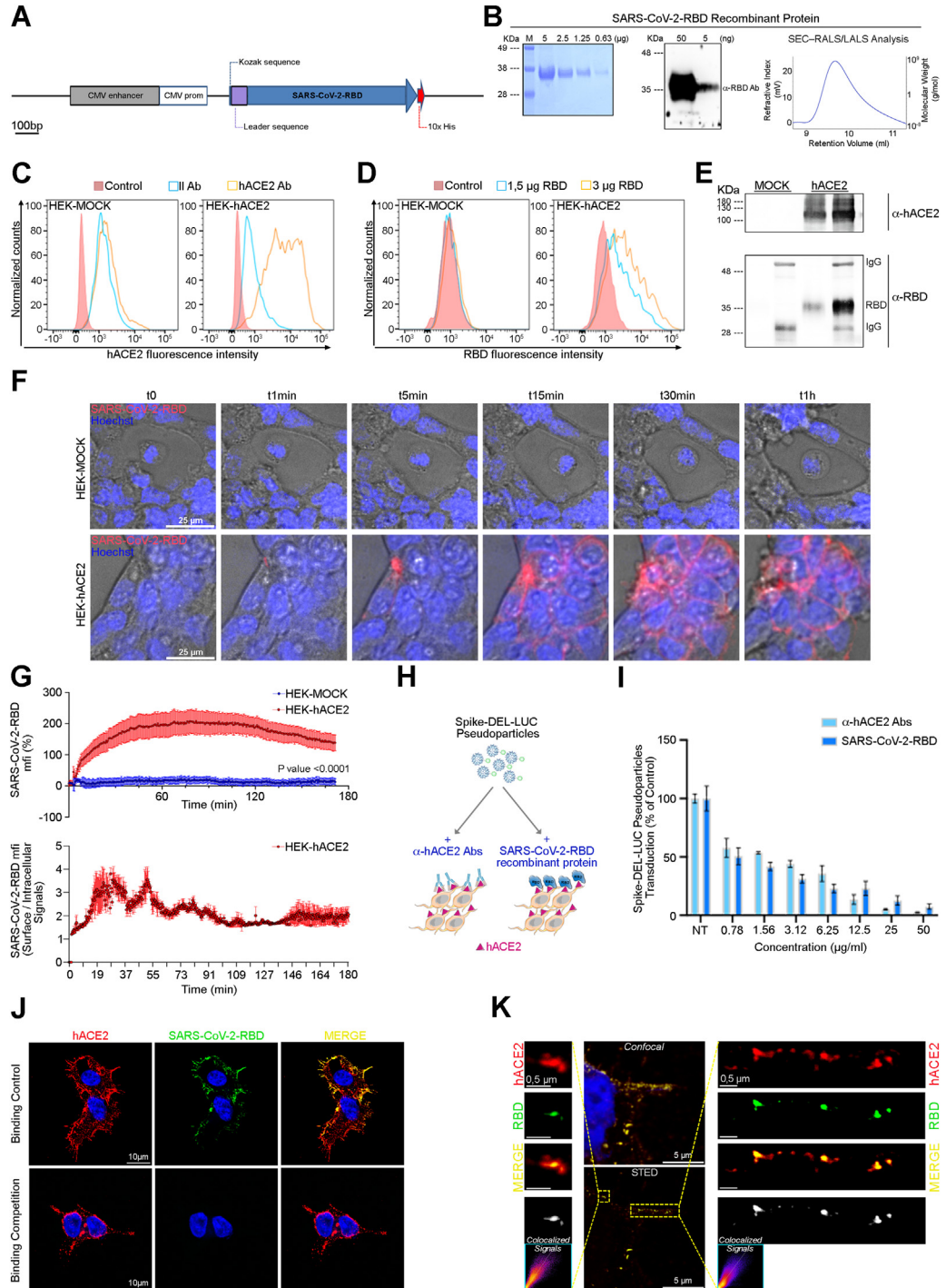


Fig. 1: SARS-CoV-2-RBD binds a subset of plasma-membrane hACE2 receptors. (A–E) Validation of SARS-CoV-2-RBD binding to living epithelial cells. (A) Scheme describing recombinant SARS-CoV-2-RBD. (B) Left, SDS-PAGE analysis of purified SARS-CoV-2-RBD recombinant protein (~36 kDa) visualized through Coomassie blue staining. Marker is indicated (M). Middle, Western blot of recombinant SARS-CoV-2-RBD protein. Right, SEC-RALS/LALS analysis of SARS-CoV-2-RBD recombinant protein. The Coomassie stain, Western blot and SEC-RALS/LALS are representative of three independent experiments. (C) FACS analysis of HEK 293 T cells transiently transfected with a plasmid encoding for hACE2 (HEK hACE2) or with an empty vector (HEK MOCK). Graphs are representative of three independent experiments. (D) FACS analysis of HEK 293 T cells transiently expressing hACE2 compared to the MOCK controls. Samples were stained with two concentrations of fluorescently labeled SARS-CoV-2-RBD. Graphs are representative of three independent experiments. (E) hACE2- SARS-CoV-2-RBD co-IP. Protein lysates

entry by antibody-blockade of ACE2 (Fig. 1I), as expected. In short, SARS-CoV-2-RBD binding predicts viral interaction.

Having established that SARS-CoV-2-RBD binding predicts viral interaction, we asked whether hACE2 expression totally predicts SARS-CoV-2-RBD binding. At first, we performed confocal imaging of hACE2-expressing HEK293T cells incubated with saturating concentrations of fluorescent SARS-CoV-2-RBD. We found that hACE2 and SARS-CoV-2-RBD co-localized on the external part of the cell membrane (Fig. 1J, top), as expected. Binding competition assays with a three-fold concentration of the unlabeled SARS-CoV-2-RBD abolished fluorescent SARS-CoV-2-RBD staining (Fig. 1J, bottom and Fig. S3A and S3B, bottom). However, a significant amount of hACE2 did not overlap with fluorescent SARS-CoV-2-RBD, suggesting that the presence of hACE2 is necessary but not sufficient for SARS-CoV-2-RBD binding (Fig. 1J, top, Fig. S3A and S3B, top; Fig. S3C and S3D, and Movies S8 and S9).

To further define the topological relationship between hACE2 expression and SARS-CoV-2-RBD binding, we analyzed the binding by fluorescent STimulated Emission Depletion (STED) super resolution microscopy. We found that: i) interaction between hACE2 and SARS-CoV-2-RBD is restricted to the cell surface, ii) SARS-CoV-2-RBD signals co-localize with hACE2 signals, but iii) not all hACE2 receptors are bound to SARS-CoV-2-RBD, as only part of hACE2 signals overlap with fluorescent-SARS-CoV-2-RBD spots (Fig. 1K and Fig. S3E and S3F). Taken together these data suggest that a pool of hACE2 receptors is either not available or not actively competent for SARS-CoV-2-RBD binding.

hACE2 levels do not suffice for SARS-CoV-2-RBD binding in human lung tissues

Next, we asked whether hACE2 expression and SARS-CoV-2-RBD binding in human tissues showed evidence

of partial overlap. We analyzed normal lung tissues derived from the biopsies of six patients with pathologies not related to COVID-19, as summarized in Fig. 2A. 5 μ m-thick frozen lung sections were fixed, stained with hematoxylin and eosin for morphological evaluation, and subjected to double staining with labeled-SARS-CoV-2-RBD and anti-hACE2 antibodies (Fig. 2B). Fig. 2C and Fig. S4A show representative images taken across six individuals. The analysis of multiple fields showed that: a) different patients had drastically different levels of hACE2 protein (Fig. 2C and Fig. S4A–S4C); b) hACE2⁺ spots were not always matched by SARS-CoV-2-RBD signals (Fig. 2C and Fig. S4A and S4D); c) SARS-CoV-2-RBD binding was always dependent on the presence of hACE2. Pre-incubation with unlabeled SARS-CoV-2-RBD completely abolished fluorescent SARS-CoV-2-RBD staining (Fig. S4E and S4G), confirming the specificity of our SARS-CoV-2-RBD labeling also on frozen tissues.

To further define the topological relationship between hACE2 expression and SARS-CoV-2-RBD binding, we quantitated the percentage of hACE2/SARS-CoV-2-RBD double positive spots/field tissue (Fig. 2D). By performing Pearson correlation analysis between hACE2 and SARS-CoV-2-RBD we found that colocalization of the two molecules differed among the six lung tissues, due to patient-to-patient variability (Fig. 2E). To overcome the auto-fluorescence noise typical of frozen lung samples, which partially restricts sensitivity of classical confocal microscopy, we performed a sequential scanning of central focal Z-planes of either the entire epithelial cell(s), by confocal microscopy following 3D image processing (Fig. 2F, top and right insets), or of specific SARS-CoV-2-RBD/hACE2 spots, by STED microscopy (Fig. 2F, bottom). Clearly, the presence of hACE2 is required but not sufficient for SARS-CoV-2-RBD binding, as SARS-CoV-2-RBD spots always co-localized with hACE2 spots but were less abundant. During infection,

derived from the samples described in (C) were immunoprecipitated with anti-hACE2 antibodies. Blots are representative of three independent experiments. (F) Captured images of selected cropped areas from live-cell imaging experiment on both HEK-MOCK and HEK-hACE2 expressing cells. Nuclei were stained with Hoechst 33342. Scale bars are indicated. (G) Mean fluorescence intensity of SARS-CoV-2-RBD protein signals over time. Top, measurement of fluorescently labeled-SARS-CoV-2-RBD signals in HEK-hACE2 cells, at the indicated time after protein binding. Bottom, same data as above but expressed as the Ratio between plasma membrane and intracellular compartment signals. Data are expressed as mean \pm SEM (top, n = 6 FOVs each; bottom, n = 3 FOVs each). (Non parametric Kruskal-Wallis test, p-value <0.0001, ****) (H) Scheme describing the binding competition assay based on SARS-CoV-2 pseudoparticle infection. Prior to infection with SPIKE-DEL-LUC pseudoparticles, Vero cells expressing endogenous ACE2, were incubated with either anti-hACE2 antibodies or recombinant SARS-CoV-2-RBD. (I) Pseudoparticles transduction efficiency in Vero cells is reduced by SARS-CoV-2-RBD competition. Cells were treated as described in (F) and transduced with 10MOI of SPIKE-DEL-LUC pseudoparticles. Histograms represent means \pm SD of three independent experiments. NT = cells not pre-treated with SARS-CoV-2-RBD or anti-hACE2 antibodies. (J) Confocal microscopy images of HEK 293 T cells expressing hACE2 and the binding of SARS-CoV-2-RBD. Prior to staining with fluorescently labeled SARS-CoV-2-RBD (green) and anti-hACE2 antibodies (red), cells were either left untreated (top) or pre-incubated with saturating concentrations of unlabeled recombinant SARS-CoV-2-RBD (bottom). Colocalized signals in yellow. Scale bars are indicated. (K) Confocal and STED images of one selected hACE2-HEK cell. Lower magnification (Center). hACE2 (red) and SARS-CoV-2-RBD (green) signals were detected as described in (H). Scale bars are indicated. Right and left: two enlarged areas show the co-localization (yellow) between hACE2 (red) and SARS-CoV-2-RBD (green) on the cell surface. Scale bars are indicated. Yellow signals were better evidenced by grey-co-localized pixels and by colocalization map. Scatterplots represent the distribution of hACE2 (red) and SARS-CoV-2-RBD (green) signals on the regression line.

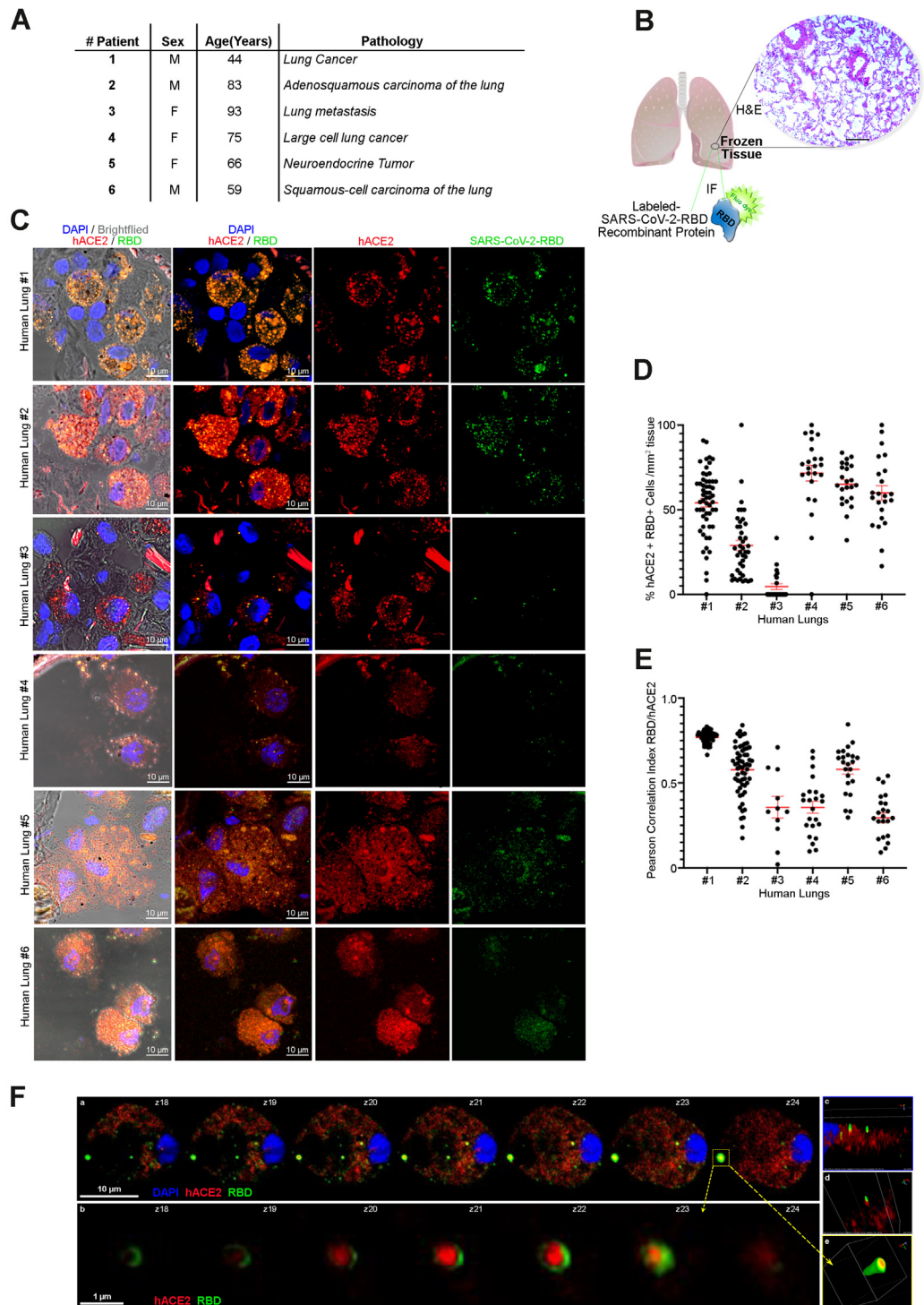


Fig. 2: The correlation between hACE2 levels and SARS-CoV-2-RBD binding in human lung tissues is highly variable. (A) List of patients analyzed. (B) Cartoon describing our tissue-derived sample processing/staining approach. Sections of frozen normal lung tissue samples derived from the biopsies of patients described in (A) were stained with hematoxylin and eosin and then labeled with fluorescent SARS-CoV-2-RBD. (C) Representative confocal microscopy images of lung tissue samples. hACE2 was detected with goat-anti-hACE2 primary antibodies and Alexa-Fluor 568-labelled anti-goat secondary antibodies (red). 647-labelled SARS-CoV-2-RBD recombinant protein was used (green). Colocalization signals in yellow. Nuclei were stained with DAPI. (D-E) Quantitation of SARS-CoV-2-RBD and hACE2 binding shows huge differences among

the SARS-CoV-2-S protein binds to hACE2 receptors in the form of a trimer. To exclude the possibility that lack of total overlap between recombinant SARS-CoV-2-RBD and hACE2 receptors could be due to a lower affinity of the monomeric form of the protein, we performed binding experiments using the SARS-CoV-2-S-Trimer. High resolution binding studies confirmed that the overlap between hACE2 and SARS-CoV-2-S-Trimer was not total (Fig. S5A). Quantitation confirmed the absence of total overlap between SARS-CoV-2-S-Trimer and hACE2 (Fig. S5B and S5C). In conclusion, the detection of conspicuous locations positive for hACE2, but negative for SARS-CoV-2-RBD staining, suggests the presence of factors that may modulate the binding of SARS-CoV-2-RBD to hACE2.

The hACE2/SARS-CoV-2-RBD interactome establishes hACE2 co-factors important for viral binding

The previous conclusions prompted us to quantify if other interactors could modulate SARS-CoV-2-RBD binding to hACE2 at the plasma membrane surface. We developed a proteomic strategy to identify them. Practically, the interactome of hACE2 was established either in the presence or absence of SARS-CoV-2-RBD. To enhance and stabilize interactions, cells were treated with DSS (Disuccinimidyl suberate), a crosslinker which reacts with primary amines. Co-Immunoprecipitations (Co-IPs) were then performed using anti-hACE2 antibodies and interactomes were defined by mass spectrometry analysis (Table S1). We found 90 proteins enriched in the hACE2/SARS-CoV-2-RBD pulldown compared to the interactome of hACE2 alone (Fig. 3A). By Gene Ontology (GO) analysis, we found these proteins to be involved in protein localization and viral processes (Fig. 3B). Among them, we found membrane-bound proteins which included several SoLute Carriers (SLCs), suggesting that SARS-CoV-2-RBD interaction with hACE2 occurs in a context of transmembrane proteins important for establishing receptor localization (Fig. 3C). We crossed our protein list with previously published interactomes of SARS-CoV-2 using the BioGRID database²⁹ and associated a score to each protein based on the total number of interactions, corrected by the number of specific interactions with the SARS-CoV-2-S protein (Fig. 3D and Table S2), as detailed in the

material and methods section. We found that SLC1A5,³⁰ SoLute Carrier family 1 Member 5, was the plasma membrane protein receptor with the highest interaction score. Intriguingly, BSG⁶ and SR-B1,³¹ two recently characterized receptors modulating SARS-CoV-2 viral entry, were among our top 5 hits, confirming the efficacy of our approach. Overall these data suggest that hACE2 binding to SARS-CoV-2-RBD is affected by neighbouring proteins.

SLC1A5 is a sodium-dependent neutral amino acid transporter required for physiological import of glutamine, asparagine, branched-chain and aromatic amino acids.³⁰ SLC1A5 was previously shown to favor viral entry of some retroviruses.^{32–35} We confirmed the interaction of SLC1A5 with both hACE2 and SARS-CoV-2-RBD by Co-IP, performing either SLC1A5 pulldown followed by western blotting (Fig. 3E) or hACE2 pull-down in the presence of high SLC1A5 levels (Fig. S6A). We found that SLC1A5 is a positive modulator of SARS-CoV-2-RBD binding. In addition, we confirmed the close apposition of SLC1A5 with ACE2 by confocal microscopy in HEK293T and Vero cells (Fig. 3F and Fig. S6B). Next, we asked to which extent SARS-CoV-2-RBD binding correlated with ACE2/SLC1A5 double positive spots. We found an evident correlation between SARS-CoV-2-RBD signals and the expression of both ACE2 and SLC1A5 (Fig. 3G, top and Fig. S6C), suggesting an increased availability of the ACE2 receptor for the SARS-CoV-2-RBD protein when the former is bound to SLC1A5. Several double ACE2/SLC1A5 spots without SARS-CoV-2-RBD were also detectable, as well as a minority of SARS-CoV-2-RBD/ACE2 spots without SLC1A5, indicating that SLC1A5 is not uniquely necessary for SARS-CoV-2-RBD binding to ACE2, but may function by stabilizing the SARS-CoV-2-RBD/ACE2 complex and/or facilitating SARS-CoV-2-RBD/ACE2 interaction. To verify this hypothesis, we performed Pearson correlation analysis between SLC1A5, ACE2 and SARS-CoV-2-RBD in triple-positive spots. The analysis of SARS-CoV-2-RBD positive spots resulted in 0.6 Pearson correlation between ACE2 and SLC1A5 signals. In the absence of SARS-CoV-2-RBD, the correlation decreased to 0.2. In summary, we conclude that SARS-CoV-2-RBD interacts with ACE2 preferentially when the latter is closely bound to SLC1A5 (Fig. 3G, bottom and Fig. S6C and S6D).

patients in the relationship between hACE2 expression as detected by immunohistochemistry and SARS-CoV-2-RBD binding. (D) Quantitation of double positive cells in each lung tissue sample. Graph represents the percentage of SARS-CoV-2-RBD and hACE2 double positive cells per mm² of tissue. Each dot represents the percentage of double positive cells per Field of View (n = 58 FOVs/samples #1; n = 41 FOVs/samples #2; n = 23 FOVs/samples #3–#6). Means ± SEM are indicated. (E) SARS-CoV-2-RBD and hACE2 colocalization was analyzed by Pearson Correlation Index. Each dot represents the pixel-wise colocalization signal. Means ± SEM are indicated (n = 60 analyzed co-labelled spots/samples #1–#3; n = 23 analyzed co-labelled spots/sample #4–#6). (F) Representative microscopy images of one selected human lung epithelial cell. (a) Confocal image showing 7 central Z-steps sequentially acquired. (b) STED image showing the same 7 central Z-steps, but focusing on the major spot of interaction between hACE2 and SARS-CoV-2-RBD, as indicated in the yellow box in A. Selected frames extracted from 3D-reconstructed movies of small spots (c, d) and of the major spot (e). Scale bars are indicated.

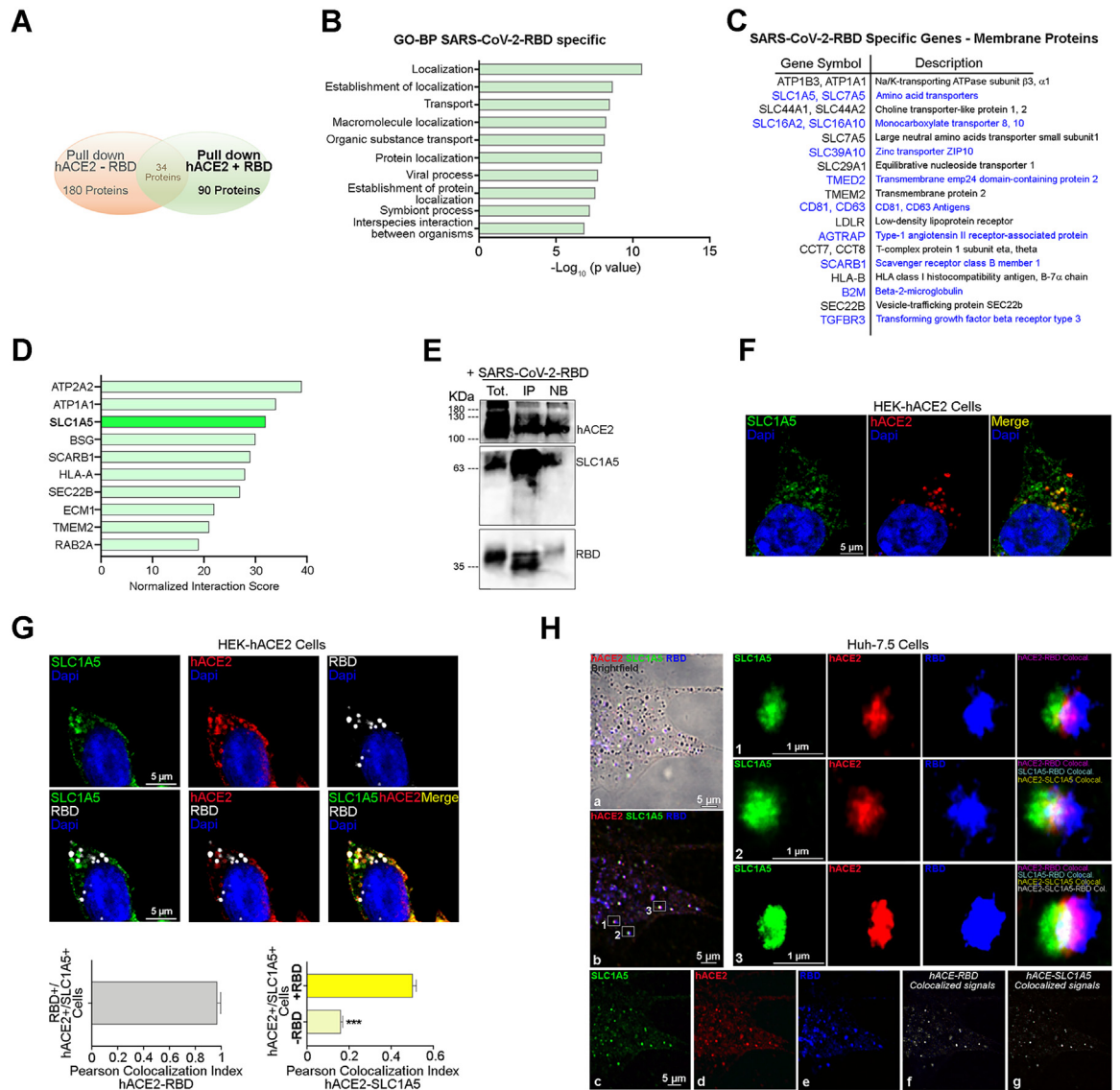


Fig. 3: SLC1A5 interacts with hACE2/SARS-CoV-2-RBD in human cell lines. (A) Total number of proteins detected by mass spectrometry, upon hACE2 pulldown with or without SARS-CoV-2-RBD. (B) GO enrichment analysis of proteins specific of the hACE2 + SARS-CoV-2-RBD pulldown. (C) List of membrane proteins specific for the hACE2 + SARS-CoV-2-RBD pulldown. (D) Top 10 interactors of hACE2 in the presence of SARS-CoV-2-RBD. The 90 proteins specific of the hACE2 + SARS-CoV-2-RBD pulldown were crossed with previously published SARS-CoV-2 interactomes and each protein was given a score (refer to the “Methods” section for details). (E) SLC1A5 was immunoprecipitated from HEK-hACE2 cells, previously incubated with recombinant SARS-CoV-2-RBD protein, using anti-SLC1A5 antibodies. The blot is representative of three independent experiments. (F) hACE2 and SLC1A5 colocalization in HEK cells. Confocal microscopy images obtained from hACE2-HEK cells stained with anti-hACE2 (red) and anti-SLC1A5 (green) antibodies. Nuclei were stained with DAPI. Scale bars are indicated. (G) hACE2, SLC1A5 and SARS-CoV-2-RBD colocalization in HEK cells. Top, hACE2 (red) and SLC1A5 (green) proteins were stained as in (F). 647-labelled-SARS-CoV-2-RBD is shown in white. Nuclei were stained with DAPI. Scale bars are indicated. Bottom, Pearson correlation index between hACE2 and SARS-CoV-2-RBD (n = 28 co-labeled spots) and between hACE2 and SLC1A5 either in the presence or absence of SARS-CoV-2-RBD (n = 100 co-labeled spots/sample). (Kruskal–Wallis test, p-value <0.001, ***). (H) Representative confocal image of Huh-7.5 cells, incubated in live with 647-labeled SARS-CoV-2-RBD protein. Immunofluorescence staining was performed as described in (G); (a-e) images of single and multiple spots at lower magnification. Scale bars are indicated. (f-g) Images showing the colocalization signals between hACE2 and SAR-CoV-2-RBD (grey). (1–3) boxes representing the spatial interaction between hACE2, SLC1A5 and SARS-CoV-2-RBD proteins by 2D reconstruction on a single Z-plan. Scale bars are indicated.

In order to see if SLC1A5 may act as a stabilizer for hACE2/SARS-CoV-2-RBD interaction, we performed a binding assay in living cells. We selected Huh-7.5 cells due to their high SLC1A5 levels (Fig. S6E and S6F), and carried out immunofluorescence staining for both hACE2 and SLC1A5. We found that the three proteins were consistently in the same spatial compartment (Fig. 3H, panels a–g and Fig. S6G). Notably, SARS-CoV-2-RBD spots were detectable only when both hACE2 and SLC1A5 protein signals coexisted. By 2D reconstruction on a single Z-plan, we found that the hACE2 receptor binds its co-factor SLC1A5 on one side, and its ligand SARS-CoV-2-RBD on the opposite (Fig. 3H, panels 1–3). The topological relationship between hACE2, SLC1A5 and SARS-CoV-2-RBD binding was further explored and quantified in patient-derived normal lung tissues by conventional laser-scanning confocal (Fig. 4A–E and Fig. S7 and Fig. S8A–S8C), video-confocal-structure illumination super resolution (Fig. 4F) and STED microscopy (Fig. 4G–H). We observed that: i) SLC1A5 positive cells correlate with SARS-CoV-2-RBD binding (Fig. 4B–D and Fig. S8B and S8C), ii) lung tissues with the lowest expression of SLC1A5, i.e. those derived from patients #3 and #6 (Fig. 4A and B), are also those with less hACE2/SARS-CoV-2-RBD colocalization (Fig. 2C), although iii) SLC1A5 and SARS-CoV-2-RBD signals do not always overlap (Fig. 4E and H). Taken together, our results show that SLC1A5 is required for efficient SARS-CoV-2-RBD binding and may promote or act as a stabilizer for hACE2/SARS-CoV-2-RBD interaction *ex situ*.

SLC1A5 expression increases SARS-CoV-2 viral entry

To evaluate the importance of SLC1A5 in SARS-CoV-2-RBD interaction with host cells, we generated Huh-7.5 cell lines with stable SLC1A5 knockdown (Fig. S9A–S9D) and analyzed SARS-CoV-2-RBD binding capability by fluorescence microscopy (Fig. 5A). In SLC1A5 downmodulated cells, SARS-CoV-2-RBD binding was diminished (Fig. 5A) and triple hACE2/SARS-CoV-2-RBD/SLC1A5 co-localization was lost (Fig. 5B). Pearson correlation analyses revealed that SARS-CoV-2-RBD/hACE2 colocalization in SLC1A5 positive spots was 0.8 in control cells and dropped to 0.25 in SLC1A5 downmodulated cells (Fig. 5C). hACE2/SLC1A5 double positive spots were significantly higher in the presence of SARS-CoV-2-RBD, and diminished in the absence of SARS-CoV-2-RBD (Fig. 5D), supporting the idea that SARS-CoV-2-RBD binds the hACE2 receptor more efficiently when the latter is close to its co-factor SLC1A5. To confirm this, we assessed the binding efficiency between SARS-CoV-2-RBD and hACE2 through ELISA. The downmodulation of SLC1A5 diminished SARS-CoV-2-RBD binding to hACE2 (Fig. 5E) and such reduction was proportional to SLC1A5 downmodulation (Fig. S9A). Next, we tested if SLC1A5 could modulate viral infection. To this end, we selected Huh-7.5 cells,

given their higher expression of SLC1A5 (Fig. S6E and S6F) and higher infectability compared to Vero cells (Fig. S9E). We downmodulated SLC1A5 and infected cells with lentiviral particles pseudotyped with the SARS-CoV-2 S protein (Fig. 5F). Downregulation of SLC1A5 caused a decrease in pseudoparticle infection (Fig. 5G). Defective viral entry was not ascribable to differential cell survival (Fig. S9F). In conclusion, SLC1A5 increases both SARS-CoV-2-RBD binding to hACE2 and pseudoparticle viral entry.

We tested whether the role of SLC1A5 as an amino acid transporter could be the determinant of its pro-viral binding. To do so, we used the V-9302 compound, a competitive small molecule antagonist of SLC1A5 transmembrane glutamine flux.³⁶ We treated Huh-7.5 cells with low concentrations of V-9302 (15 μ M) for 3 h and analyzed, at first, SARS-CoV-2-RBD binding by ELISA. Surprisingly, treatment with V-9302 did not reduce, but actually increased, SARS-CoV-2-RBD binding (Fig. 5H). This result was confirmed when we analyzed SARS-CoV-2 pseudoparticle infectivity. We found a significant increase of viral entry in Huh-7.5 cells treated with V-9302 compared to untreated controls (Fig. 5I and Fig. S9G). Such effect was not correlated to drug cytotoxicity, as cell viability was comparable in the treated and untreated samples (Fig. S9H and S9I), but rather depended on a direct effect on SLC1A5. It was demonstrated that V-9302 treatment causes SLC1A5 protein stabilization,³⁶ so we speculated that increased SLC1A5 levels could explain the augmented infectability of cells upon V-9302 administration. We confirmed the increase of SLC1A5 protein levels after V-9302 treatment. In addition, by cell fractioning and FACS analysis, we also found that the protein was enriched at the membrane compartment (Fig. 5J and Fig. S9J). These results corroborate the hypothesis that increased SLC1A5 levels at the plasma membrane favor SARS-CoV-2-RBD/hACE2 interaction.

To confirm the relevance of our findings we tested if SLC1A5 was important for actual SARS-CoV-2 virus entry into host cells. We infected Huh-7.5 and Calu-3 cells, either downmodulated for SLC1A5 or pre-treated with V-9302, with pandemic human SARS-CoV-2 (isolate SARS-CoV-2/human/ITA/Milan-UNIMI-1/2020, GenBank: MT748758, B.1.1.10 variant) and found a) a decrease of viral entry in cells with SLC1A5 downmodulation and b) an increase in viral entry after V-9302 administration (Fig. 5K and Fig. S9K–S9P).

From the onset of COVID-19, the SARS-CoV-2-S protein mutated frequently in order to evade the host immune system.³⁷ The most recent SARS-CoV-2 variant family, termed OMICRON, displays a Spike protein harboring 30 core aa substitutions compared to the original SARS-CoV-2-S.³⁸ Fifteen of these substitutions fall in the RBD³⁹ and nine localize in the binding footprint of hACE2.⁴⁰ Hence, we asked whether the findings described thus far also held true for the highly

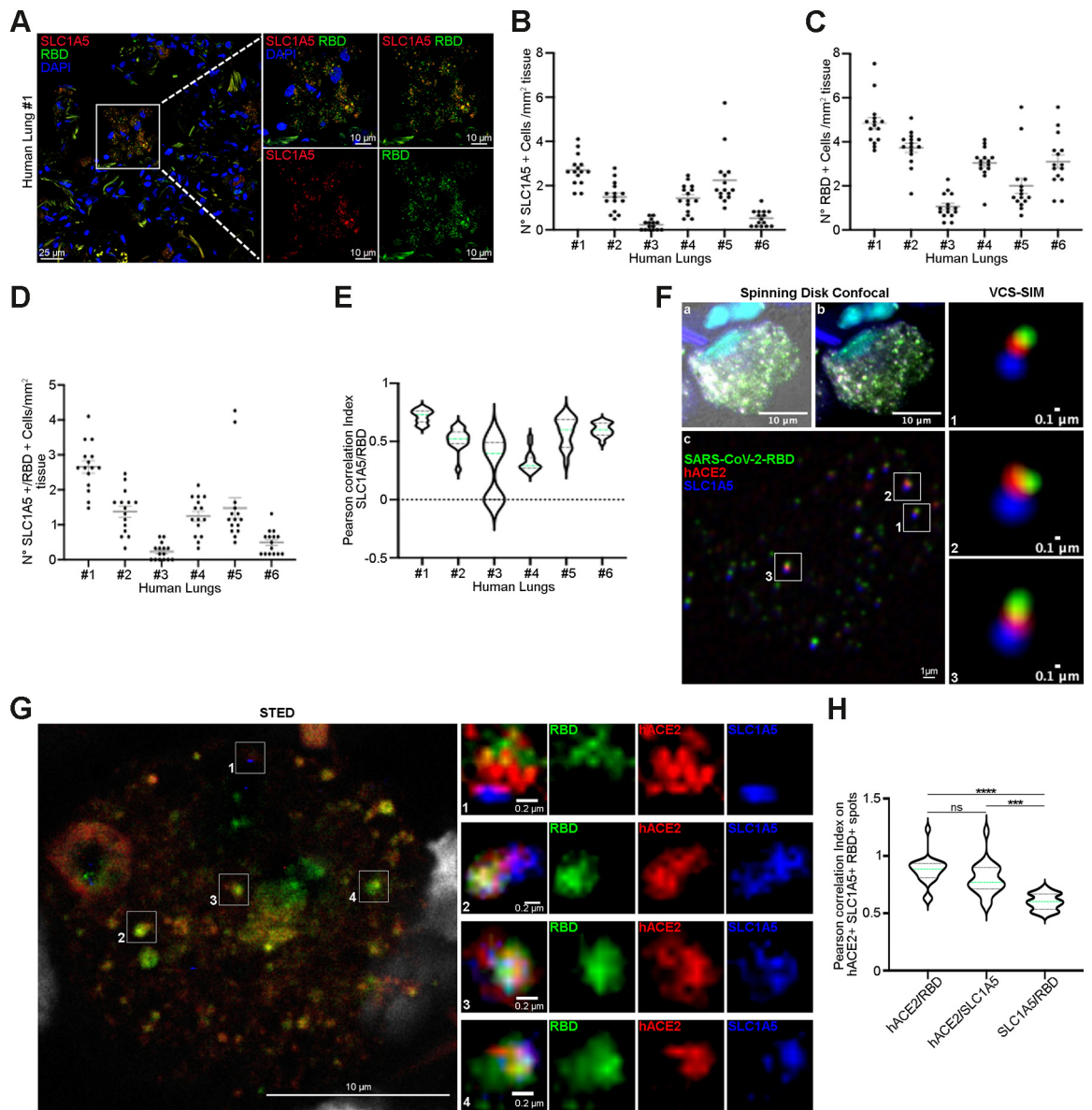


Fig. 4: SLC1A5 partly colocalizes with SARS-CoV-2-RBD in human lung tissues. (A) Representative images of normal lung tissues derived from patients listed in Fig. 2A. SLC1A5 was detected with rabbit-anti-SLC1A5 primary antibodies and Alexa-Fluor 568-labeled anti-rabbit secondary antibodies (red). 647-labeled SARS-CoV-2-RBD was used (green). Colocalized signals are shown in yellow. Nuclei were stained with DAPI. Scale bars are indicated. (B) Quantification of SLC1A5 positive cells per mm² of tissue. Each dot represents the number of positive cells/Field of View (n = 15 FOVs/sample). Means ± SEM are indicated. (C) Quantification of SARS-CoV-2-RBD positive cells per mm² of tissue. Each dot represents the number of positive cells/Field of View (n = 15 FOVs/sample). Means ± SEM are indicated. (D) Quantification of SLC1A5 and SARS-CoV-2-RBD double positive cells in each analyzed lung tissue sample. Graphs represent the number of SARS-CoV-2-RBD and hACE2 double positive cells/mm² of tissue. Each dot represents the number of double positive cells/Field of View (n = 15 FOVs/sample). Means ± SEM are indicated. (E) Pearson correlation index between SLC1A5 and SARS-CoV-2-RBD represented by Violin plots. Medians are shown in green (n = 15 analyzed pixels/FOVs/samples). (F-G) Representative images of one selected cell from the human lung tissue of individual #1 acquired with Spinning Disk video-confocal structure illumination (VCS-SIM) (F) and STED (G) microscopy. hACE2 and SLC1A5 proteins are shown in red and blue, respectively. 647-labelled-SARS-CoV-2-RBD is shown in green. Nuclei were stained with DAPI. Scale bars are indicated. All boxes represent the spatial interaction between hACE2, SLC1A5 and SARS-CoV-2-RBD proteins by 2D rendering on a single Z-plan at higher magnification. (H) Pearson correlation index represented by Violin plots. Medians are shown in green (n = 22 analyzed triple positive spots). (Kruskal-Wallis test, p-value <0.001, ***, p-value <0.0001, ****).

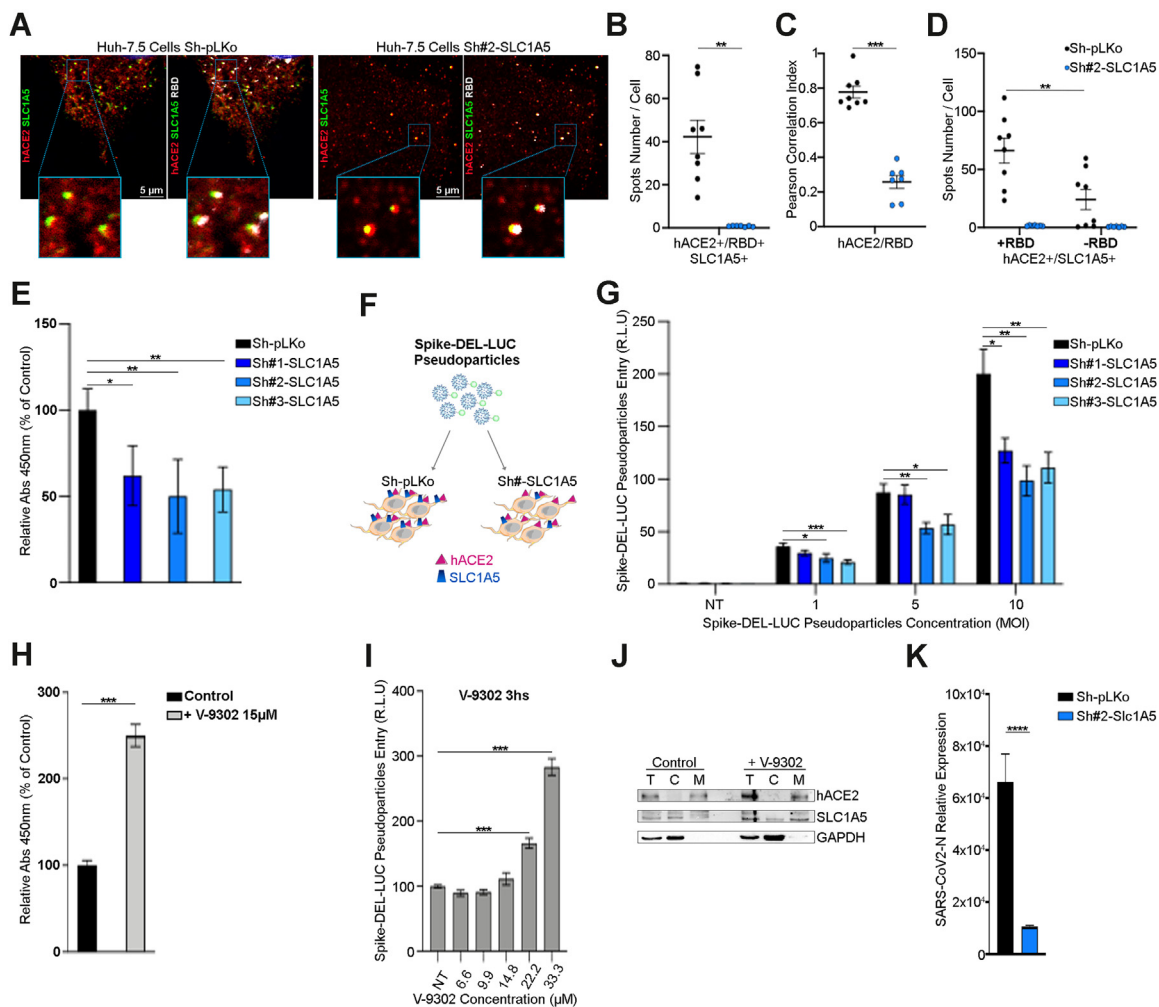


Fig. 5: SLC1A5 is required for efficient entry of pandemic SARS-CoV-2 D614G into host cells. (A) Confocal microscopy images of Huh-7.5 cells. Control (Sh-pLKO) and SLC1A5 downmodulated (Sh#-SLC1A5) cells were stained with anti-hACE2 (red), anti-SLC1A5 (green) and 647-labeled SARS-CoV-2-RBD (white). Scale bars are indicated. (B) Graph representing the number of hACE2, SLC1A5 and SARS-CoV-2-RBD triple positive spots/cell, Means \pm SEM are indicated. (Two-tailed t-test p -values: **, <0.01). (C) Pearson correlation between hACE2 and SARS-CoV-2-RBD Means \pm SEM are indicated. (p -values were calculated using two-tailed t tests: ***, <0.001). (D) Graph representing the number of hACE2/SLC1A5 double positive spots/cell in the presence or absence of SARS-CoV-2-RBD. Means \pm SEM are indicated. (p -values were calculated using two-way ANOVA ***, <0.001). For A-D a total of $n = 8$ cells/Sh-pLKO and $n = 7$ cells/Sh#2-SLC1A5 were analyzed over two independent experiments. (E) SARS-CoV-2-RBD quantitative binding to cells by ELISA assay. Data are expressed as percentages referred to Sh-pLKO signals and represent means \pm SD of three independent experiments. (p -values were calculated using two-tailed t-tests: *, <0.05 ; **, <0.01 ; ***, <0.001). (F) Scheme describing our experimental approach. Cells expressing either physiological or reduced levels of SLC1A5 were transduced with Spike-DEL-LUC pseudoparticles and assessed for viral entry. (G) Spike-DEL-LUC pseudoparticle assay. Samples prepared as in (F) were analyzed for luciferase signal intensity. Huh-7.5 cells were either infected with the indicated pseudoparticles concentrations or left untreated (NT). Histograms represent means \pm SEM of three independent experiments. (Two-tailed t-test p -values: *, <0.05 ; **, <0.01 ; ***, <0.001). (H) SARS-CoV-2-RBD binding assay in Huh-7.5 cells treated with V-9302. Data are expressed as percentages referred to the signals of control cells and represent means \pm SD of three independent experiments. (Two-tailed t-test p -value ***, <0.001). (I) Spike-DEL-LUC pseudoparticles entry assay on Huh-7.5 cells treated with increasing concentrations of V-9302. Not Treated cells (NT) values were set at 100%. Data are expressed as means \pm SEM ($n = 3$). (Two-tailed t-test p -value ***, <0.001). (J) Western blot analysis on total (T), cytosolic (C) and membrane (M) fractions of Huh-7.5 cells treated *in vitro* with either 15 μ M V-9302 or DMSO as a control. GAPDH: cytosolic control; hACE2: membrane control. (K) SARS-CoV-2 viral entry assay in Huh-7.5 cells with SLC1A5 downmodulation. Cells transduced with either control plasmid Sh-pLKO or Sh#2-SLC1A5, were infected with 0.1 MOI of SARS-CoV2 viral particles. Histograms represent the relative expression levels. Means \pm SD ($n = 4$) are shown. (Two-tailed t-test p -value: ****, <0.0001).

mutated Omicron Spike variant (hereinafter referred to as SARS-CoV-2-S-Omicron). At first, we expressed SARS-CoV-2-S-Omicron B.1.1.529 (Fig. 6A) in eukaryotic cells and purified it from the supernatant (Fig. 6B). Then, to assess its specificity, we tested its binding to the cell surface of either hACE2-expressing or MOCK control HEK293T cells. We confirmed that the presence of hACE2 was required for OMICRON BA.1 SARS-CoV-2-S binding (Fig. 6C). Next, by quantifying the number of cells positive for SARS-CoV-2-S staining we compared the binding efficiency of SARS-CoV-2-S-Omicron with that of original SARS-CoV-2-RBD. Using equal amounts of the recombinant proteins, we found that SARS-CoV-2-S-Omicron had a higher binding efficiency compared to SARS-CoV-2-RBD (Fig. 6D), a result in line with the higher infectivity of OMICRON B.1.1.529 compared to previous SARS-CoV-2 variants.

Next we tested SARS-CoV-2-S-Omicron binding on the previously described frozen lung tissues (Fig. 6E) and analyzed colocalization with hACE2 and SLC1A5. Performing a triple staining for hACE2, SLC1A5 and SARS-CoV-2-S-Omicron, we found that despite the number of triple positive hACE2⁺/SLC1A5⁺/SARS-CoV-2-S-Omicron⁺ spots in triple positive cells was lower compared to the number of double positive hACE2⁺/SLC1A5⁺ and hACE2⁺/SARS-CoV-2-S-Omicron⁺ spots (Fig. 6F), the colocalization between SARS-CoV-2-S-Omicron and either hACE2 or SLC1A5 was comparable (Fig. 6G), confirming the actual formation of a hACE2/SLC1A5/SARS-CoV-2-S-Omicron complex. Next, we compared the binding to hACE2 of SARS-CoV-2-S-Omicron with that of monomeric SARS-CoV-2-RBD and trimeric SARS-CoV-2-S. We found that the colocalization of SARS-CoV-2-S-Omicron with hACE2 was lower compared to that of either monomeric SARS-CoV-2-RBD or trimeric SARS-CoV-2-S (Fig. 6H), but, nevertheless, the percentage of triple positive cells was much higher in the presence of the OMICRON variant (Fig. 6I). Taken together our data support the existence of a hACE2/SLC1A5/SARS-CoV-2-S-Omicron complex and confirm a more efficient binding of SARS-CoV-2-S-Omicron to hACE2 compared to both monomeric SARS-CoV-2-RBD or trimeric SARS-CoV-2-S.

Last, we checked if SLC1A5 was important for actual SARS-CoV-2-S-Omicron entry into host cells. We infected Huh-7.5 cells, either downmodulated for SLC1A5 or pre-treated with V-9302, with pandemic human SARS-CoV-2 variant B.1.1.529 (GISAID ref. seq. EPI_ISL_10898045) and quantified intracellular viral load. We actually found a decrease of viral entry in cells with SLC1A5 downmodulation and an increase in viral entry after V-9302 administration (Fig. 6J and K). Taken together our data suggest that, independent of the SARS-CoV-2 variant analyzed, high levels of SLC1A5 protein facilitate hACE2 interaction with SARS-CoV-2-S, in turn allowing efficient viral entry into host cells (Fig. 7).

Discussion

SARS-CoV-2 causes multisystem inflammatory syndromes after acute-phase infection.^{41–43} Such complications are possibly exacerbated by the capability of SARS-CoV-2 to spread and infect several organs of the body. For this reason, investigating in detail the topological distribution of SARS-CoV-2 binding sites *in vivo* is important. Here we found that a) not all detectable hACE2 is competent for SARS-CoV-2 binding, suggesting the presence of additional modulators. By proteomics and functional assays, we discovered that b) SLC1A5 membrane localization increases the presence of hACE2 receptors able to bind SARS-CoV-2-RBD. Finally, c) SARS-CoV2 variants differ in their capability to bind hACE2 receptors, possibly explaining also differences in their tropism. Overall, we suggest that the systematic, direct detection of labeled SARS-CoV-2-RBD may help to understand which cells are potentially infectable by SARS-CoV-2.

Until now hACE2 expression alone was used as a proxy for the cell types that may be infected by SARS-CoV-2. The most employed approaches were to perform either immunohistochemical studies, as *in*⁷, or to rely on mRNA studies, even at the single cell level, as *in*⁴⁴. However, these approaches wrongly rely on the assumption that the expression of the hACE2 protein in a cell is sufficient for SARS-CoV-2 binding, or that the expression of an mRNA is predictive of the expression of the correspondent protein. Concerning mRNA levels, it is well known that mRNA expression is not sufficient for predicting protein expression given the existence of a strong layer of translational control.^{45,46} Concerning the sufficiency of hACE2 expression for viral binding, we ignored the possibility that co-players may facilitate or impair the binding of viral particles, or the possibility that part of hACE2, as mapped by immunohistochemistry, is not exposed at the plasma membrane in the proper virus-binding conformation. In this context, our approach, based on the binding of labeled SARS-CoV-2-RBD to human lung tissues, allows for an efficient and faithful recapitulation of the cells that may be infected by SARS-CoV-2 *in vivo*. Among the clear advantages of our approach, the sensitivity is very high. SARS-CoV-2-RBD binding to the hACE2 receptor is strong and results in a very low signal/noise ratio, considering that the affinity is estimated at 6 nM.⁴⁷ The physiological relevance of the binding is demonstrated by the fact that unlabeled recombinant SARS-CoV-2-RBD reduces the capability of SARS-CoV-2 to infect epithelial cells with an efficiency comparable to that of blocking the hACE2 receptor with blocking antibodies. In short, our method for mapping those hACE2 receptors which are capable to be bound by SARS-CoV-2 on sections is suitable for functional studies, whereas indirect measures, such as immunohistochemistry, or even worse, single cell RNAseq studies, are not very meaningful.

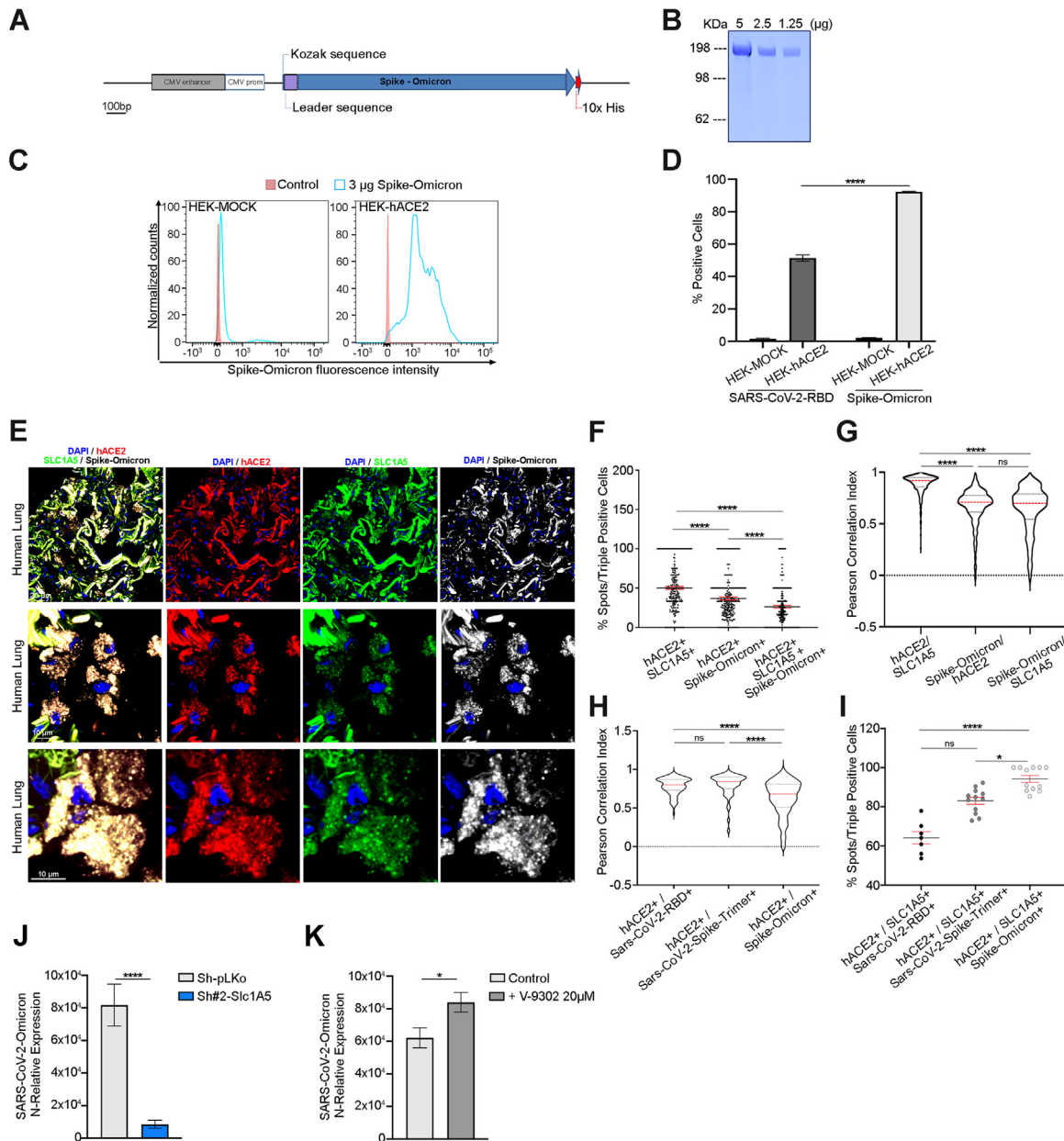


Fig. 6: SLC1A5 is required for efficient entry of pandemic SARS-CoV-2 variant B.1.1.529 into host cells. (A) Scheme describing recombinant SARS-CoV-2-S-Omicron (B.1.1.529). (B) SDS-PAGE analysis of purified SARS-CoV-2-S-Omicron recombinant protein (~196 kDa) visualized through Coomassie blue staining. (C) FACS analysis of HEK 293 T cells stably expressing hACE2 compared to the MOCK controls. Samples were stained with two 3 µg of fluorescently labeled SARS-CoV-2-S-Omicron. Graphs are representative of three independent experiments. (D) Quantitation of SARS-CoV-2-RBD⁺ and SARS-CoV-2-S-Omicron⁺ cells. HEK 293 T cells stably expressing hACE2 were stained with equal amounts (3 µg) of either recombinant SARS-CoV-2-RBD or SARS-CoV-2-S-Omicron. Histograms represent the mean ± SD percentages of cells positive for the relative staining (n = 3). (Two tailed t-test p-value <0.0001, ****). (E) Representative immunofluorescence images of human lung tissue at different magnifications: hACE2 signals are shown in red, SLC1A5 signals in green and SARS-CoV-2-S-Omicron signals in white. Scale bars are indicated. (F) Dot plots representing the percentage of hACE2/SLC1A5 double positive spots/cell, hACE2/SARS-CoV-2-S-Omicron double positive spots/cell and hACE2/SARS-CoV-2-S-Omicron/SLC1A5 triple positive spots/cell (n = 245 analyzed spots) within triple positive cells. hACE2 spots are more than SARS-CoV-2-S-Omicron spots. Means ± SEM are indicated. (Kruskal-Wallis test, p-value <0.0001, ****). (G) Pearson correlation index between the three proteins represented by Violin plots. The median is shown in red (n = 317 analyzed pixels). (Kruskal-Wallis test, p-value <0.0001, ****). (H) Pearson correlation index between the indicated proteins in triple positive cells, represented by Violin plots. Median is shown in red (n = 478 analyzed pixels). (Kruskal-Wallis test, p-value <0.0001, ****). (I) Dot plots representing the percentage of triple positive

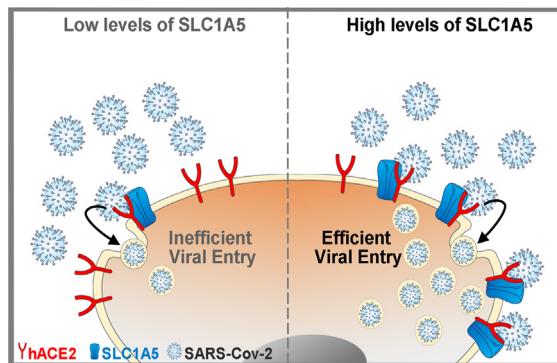


Fig. 7: Cartoon depicting our working model. High levels of SLC1A5 protein facilitate hACE2 interaction with SARS-CoV-2-S, allowing efficient SARS-CoV-2 binding and its subsequent entry into host cells.

Our binding studies suggested the existence of players that *in vivo* may contribute to SARS-CoV-2 binding. We found that several interactors of hACE2 were enriched upon SARS-CoV-2-RBD binding. Two of them, BSG⁶ and SR-B1 (SCARB1),³¹ were among our 5 top hits and have been recently characterized as co-receptors modulating SARS-CoV-2 viral entry, thus confirming the soundness of our approach. In addition, we found SLC1A5. SLC1A5 levels positively correlate with viral entry of SARS-CoV-2 variants. The tissue expression of SLC1A5 is largely overlapping with that of hACE2, with high levels observed in the respiratory and gastrointestinal tract, and in the kidney. At the cellular level, SLC1A5 is predominantly expressed on the apical membrane of ciliated epithelial bronchial cells and in alveolar cells. Overall, SLC1A5 distribution totally overlaps with known targets of SARS-CoV-2 infection, *in vivo*, suggesting a pathological relevance of its interaction with hACE2.⁴⁸ The mechanism by which SLC1A5 increases viral entry through hACE2 is not yet defined. One possibility is that SLC1A5 might further stabilize the hACE2 complex *in toto*, or preferentially steady the close conformation of the receptor, thus facilitating hACE2 interaction with SARS-CoV-2-RBD. In this context, SLC1A5 was already described as a co-interactor and stabilizing component of the BSG (CD147) complex, important for alphavirus infection.⁴⁹ The *ex situ*

relevance of SLC1A5 in viral tropism is intriguing. Given that SLC1A5 was shown to be important for viral entry of several viruses other than SARS-CoV-2,^{30,35} targeting and/or regulating the SLC1A5 protein complex could become relevant in general antiviral strategies. However, the mechanism by which SLC1A5 increases viral entry remains to be defined. Currently, we do not know if similar mechanisms are used for different viruses. Further work may address this question by defining whether SLC1A5 mutations may differentially affect viral entry.

This study has some limitations. The mapping of SARS-CoV-2-RBD binding sites in human sections represents only a snapshot of the situation that might be observed *in vivo*, in real time. For instance, it is possible that dynamic sorting of hACE2 and SLC1A5, due to membrane trafficking, continuously modifies the position and number of binding sites. This effect may occur both on a time scale of minutes, or following circadian rhythm or other undefined situations. The modulatory effect of SLC1A5 on viral entry has been shown in two conditions, one after downregulation of SLC1A5 and the second upon increased SLC1A5 localization at the plasma membrane, after pharmacological treatment. Despite being unlikely, indirect effects of the drug on hACE2 trafficking cannot be ruled out. In addition, we did not produce data with SLC1A5 overexpression since the protein is already highly abundant and the risk of heavily modifying membrane composition may lead to indirect effects.

Data sharing statement

The mass spectrometry proteomics data have been deposited to the ProteomeXchange Consortium via the PRIDE⁵⁰ partner repository with the dataset identifier [PXD038005](https://doi.org/10.26434/chemrxiv-2023-pxd03). All data presented in this manuscript are also available online as supplemental material.

Contributors

N.M., A.M. and S.B. conceived and designed the research. A.M. and N.M. performed most of the experiments and analyses. A.C. performed Mass Spectrometry. C.C. performed fluorescent microscopy analyses. L.D. generated hACE2-HEK cell lines, SARS-CoV-2-Spike pseudoparticles and performed viral entry assays. E.P. produced fluorescently-labeled SARS-CoV-RBD and performed ELISA SARS-CoV-2-RBD binding assays. M.B. designed and purified recombinant SARS-CoV-2-RBD. M.C. and A.F. designed and generated SARS-CoV-2-Spike pseudoparticles. L.M. performed viral entry assays. M.T. performed size exclusion chromatography. L.T. provided lung tissue samples. A.S., S.O.

spots in lung cells: comparison between hACE2/SARS-CoV-2-RBD/SLC1A5, hACE2/SARS-CoV-2-Spike-Trimer/SLC1A5 and hACE2/SARS-CoV-2-S-Omicron/SLC1A5 triple positive spots/cell (n = 7 analyzed cells for SARS-CoV-2-RBD experiment; n = 12 analyzed cells for SARS-CoV-2-Spike-Trimer and SARS-CoV-2-Spike-Omicron experiments). Means ± SEM are indicated. (Kruskal-Wallis test, p-value <0.05, *; p-value <0.0001, ****). (J) SARS-CoV-2-Omicron viral entry assay in Huh-7.5 cells with SLC1A5 downmodulation. Cells transfected with either control plasmid Sh-pLCo or Sh#2-SLC1A5, were infected with 0.1 MOI of OMICRON B.1.1.529 SARS-CoV2 viral particles. Histograms represent the relative mean expression levels ± SD (n = 3) of intracellular SARS-CoV-2-N. (A two tailed t-test was applied, p-value <0.0001: ****). (K) SARS-CoV-2-Omicron viral entry assay in Huh-7.5 cells treated with V-9302. Cells either left untreated or treated with 20 μM V-9302, were infected with 0.1 MOI of OMICRON B.1.1.529 SARS-CoV2 viral particles. Histograms represent the relative mean expression levels ± SD (n = 3) of intracellular SARS-CoV-2-N. (A two tailed t-test was applied, p-value <0.05: *).

and S.R. discussed the results. R.G. critically evaluated the research, designed experiments and discussed the results. R.De F. and S.A. evaluated the research and discussed the results. N.M., A.M. and S.B. wrote the paper. All authors commented on and critically revised the manuscript. SB, NM and AM have directly accessed and verified all data from the current manuscript.

Declaration of interests

The authors report no conflict of interest.

Acknowledgments

The authors wish to thank Frédéric Eghiaian from Abberior Instruments and Alessandro Rossi from Crisel Instruments, for allowing us to perform STED microscopy acquisitions with the Abberior STE-DYCON instrument. We thank Professor Serena Delbue, UNIMI for supplying SARS-CoV-2 virus.

This work was supported by an unrestricted grant from “Fondazione Romeo ed Enrica Invernizzi” to Stefano Biffo and by AIRC under MFAG 2021 - ID. 26178 project – P.I. Manfrini Nicola.

Appendix A. Supplementary data

Supplementary data related to this article can be found at <https://doi.org/10.1016/j.ebiom.2022.104390>.

References

- Garcia-Montero C, Fraile-Martinez O, Bravo C, et al. An updated review of SARS-CoV-2 vaccines and the importance of effective vaccination programs in pandemic times. *Vaccines (Basel)*. 2021;9(5).
- Robinson PC, Liew DFL, Tanner HL, et al. COVID-19 therapeutics: challenges and directions for the future. *Proc Natl Acad Sci USA*. 2022;119(15):e2119893119.
- Nalbandian A, Sehgal K, Gupta A, et al. Post-acute COVID-19 syndrome. *Nat Med*. 2021;27(4):601–615.
- Ge J, Wang R, Ju B, et al. Antibody neutralization of SARS-CoV-2 through ACE2 receptor mimicry. *Nat Commun*. 2021;12(1):250.
- Liu A, Zhang X, Li R, et al. Overexpression of the SARS-CoV-2 receptor ACE2 is induced by cigarette smoke in bronchial and alveolar epithelia. *J Pathol*. 2021;253(1):17–30.
- Essahib W, Verheyen G, Tournaye H, Van de Velde H. SARS-CoV-2 host receptors ACE2 and CD147 (BSG) are present on human oocytes and blastocysts. *J Assist Reprod Genet*. 2020;37(11):2657–2660.
- Hamming I, Timens W, Bulthuis ML, Lely AT, Navis G, van Goor H. Tissue distribution of ACE2 protein, the functional receptor for SARS coronavirus. A first step in understanding SARS pathogenesis. *J Pathol*. 2004;203(2):631–637.
- Kuba K, Imai Y, Rao S, et al. A crucial role of angiotensin converting enzyme 2 (ACE2) in SARS coronavirus-induced lung injury. *Nat Med*. 2005;11(8):875–879.
- Lely AT, Hamming I, van Goor H, Navis GJ. Renal ACE2 expression in human kidney disease. *J Pathol*. 2004;204(5):587–593.
- Mizuri S, Hemmi H, Arita M, et al. Increased ACE and decreased ACE2 expression in kidneys from patients with IgA nephropathy. *Nephron Clin Pract*. 2011;117(1):c57–c66.
- Wiener RS, Cao YX, Hinds A, Ramirez MI, Williams MC. Angiotensin converting enzyme 2 is primarily epithelial and is developmentally regulated in the mouse lung. *J Cell Biochem*. 2007;101(5):1278–1291.
- Vitale-Cross L, Szalayova I, Scoggins A, Palkovits M, Mezey E. SARS-CoV-2 entry sites are present in all structural elements of the human glossopharyngeal and vagal nerves: clinical implications. *EBioMedicine*. 2022;78:103981.
- Winkler ES, Bailey AL, Kafai NM, et al. SARS-CoV-2 infection of human ACE2-transgenic mice causes severe lung inflammation and impaired function. *Nat Immunol*. 2020;21(11):1327–1335.
- Hui KPY, Ho JCW, Cheung MC, et al. SARS-CoV-2 Omicron variant replication in human bronchus and lung ex vivo. *Nature*. 2022;603(7902):715–720.
- Notarbartolo S, Ranzani V, Bandera A, et al. Integrated longitudinal immunophenotypic, transcriptional and repertoire analyses delineate immune responses in COVID-19 patients. *Sci Immunol*. 2021;6(62).
- Manfrini N, Mancino M, Miluzio A, et al. FAM46C and FNDC3A are multiple myeloma tumor suppressors that act in concert to impair clearing of protein aggregates and autophagy. *Cancer Res*. 2020;80(21):4693–4706.
- Conforti A, Marra E, Palombo F, et al. COVID-eVax, an electroporated DNA vaccine candidate encoding the SARS-CoV-2 RBD, elicits protective responses in animal models. *Mol Ther*. 2021;30(1):311–326.
- Gallo S, Ricciardi S, Manfrini N, et al. RACK1 specifically regulates translation through its binding to ribosomes. *Mol Cell Biol*. 2018;38(23).
- Manfrini N, Ricciardi S, Miluzio A, et al. High levels of eukaryotic Initiation Factor 6 (eIF6) are required for immune system homeostasis and for steering the glycolytic flux of TCR-stimulated CD4(+) T cells in both mice and humans. *Dev Comp Immunol*. 2017;77:69–76.
- Pignatti E, Mascheroni L, Sabelli M, Barelli S, Biffo S, Pietrangelo A. Ferroportin is a monomer in vivo in mice. *Blood Cells Mol Dis*. 2006;36(1):26–32.
- Shevchenko A, Tomas H, Havlis J, Olsen JV, Mann M. In-gel digestion for mass spectrometric characterization of proteins and proteomes. *Nat Protoc*. 2006;1(6):2856–2860.
- Rappsilber J, Mann M, Ishihama Y. Protocol for micro-purification, enrichment, pre-fractionation and storage of peptides for proteomics using StageTips. *Nat Protoc*. 2007;2(8):1896–1906.
- Tyanova S, Temu T, Cox J. The MaxQuant computational platform for mass spectrometry-based shotgun proteomics. *Nat Protoc*. 2016;11(12):2301–2319.
- Cox J, Hein MY, Luber CA, Paron I, Nagaraj N, Mann M. Accurate proteome-wide label-free quantification by delayed normalization and maximal peptide ratio extraction, termed MaxLFQ. *Mol Cell Proteomics*. 2014;13(9):2513–2526.
- Tyanova S, Temu T, Sinitcyn P, et al. The Perseus computational platform for comprehensive analysis of (prote)omics data. *Nat Methods*. 2016;13(9):731–740.
- Biffo S, DeLucia R, Mulatero B, Margolis F, Fasolo A. Carnosine, calcitonin gene-related peptide- and tyrosine hydroxylase-immunoreactivity in the mouse olfactory bulb following peripheral denervation. *Brain Res*. 1990;528(2):353–357.
- Lan J, Ge J, Yu J, et al. Structure of the SARS-CoV-2 spike receptor-binding domain bound to the ACE2 receptor. *Nature*. 2020;581(7807):215–220.
- Ejemel M, Li Q, Hou S, et al. A cross-reactive human IgA monoclonal antibody blocks SARS-CoV-2 spike-ACE2 interaction. *Nat Commun*. 2020;11(1):4198.
- Oughtred R, Stark C, Breitkreutz BJ, et al. The BioGRID interaction database: 2019 update. *Nucleic Acids Res*. 2019;47(D1):D529–D541.
- Scalise M, Pochini L, Console L, Losso MA, Indiveri C. The human SLC1A5 (ASCT2) amino acid transporter: from function to structure and role in cell biology. *Front Cell Dev Biol*. 2018;6:96.
- Wei C, Wan L, Yan Q, et al. HDL-scavenger receptor B type 1 facilitates SARS-CoV-2 entry. *Nat Metab*. 2020;2(12):1391–1400.
- Lavillette D, Marin M, Ruggieri A, Mallet F, Cosset FL, Kabat D. The envelope glycoprotein of human endogenous retrovirus type W uses a divergent family of amino acid transporters/cell surface receptors. *J Virol*. 2002;76(13):6442–6452.
- Marin M, Lavillette D, Kelly SM, Kabat D. N-linked glycosylation and sequence changes in a critical negative control region of the ASCT1 and ASCT2 neutral amino acid transporters determine their retroviral receptor functions. *J Virol*. 2003;77(5):2936–2945.
- Marin M, Tailor CS, Nouri A, Kabat D. Sodium-dependent neutral amino acid transporter type 1 is an auxiliary receptor for baboon endogenous retrovirus. *J Virol*. 2000;74(17):8085–8093.
- Yoshikawa R, Yasuda J, Kobayashi T, Miyazawa T. Canine ASCT1 and ASCT2 are functional receptors for RD-114 virus in dogs. *J Gen Virol*. 2012;93(Pt 3):603–607.
- Schulte ML, Fu A, Zhao P, et al. Pharmacological blockade of ASCT2-dependent glutamine transport leads to antitumor efficacy in preclinical models. *Nat Med*. 2018;24(2):194–202.
- Li J, Lai S, Gao GF, Shi W. The emergence, genomic diversity and global spread of SARS-CoV-2. *Nature*. 2021;600(7889):408–418.
- Ou J, Lan W, Wu X, et al. Tracking SARS-CoV-2 Omicron diverse spike gene mutations identifies multiple inter-variant recombination events. *Signal Transduct Target Ther*. 2022;7(1):138.

- 39 Shrestha LB, Foster C, Rawlinson W, Tedla N, Bull RA. Evolution of the SARS-CoV-2 omicron variants BA.1 to BA.5: implications for immune escape and transmission. *Rev Med Virol*. 2022:e2381.
- 40 Dejinirattisai W, Huo J, Zhou D, et al. SARS-CoV-2 Omicron-B.1.1.529 leads to widespread escape from neutralizing antibody responses. *Cell*. 2022;185(3):467–484.e15.
- 41 Abrams JY, Godfred-Cato SE, Oster ME, et al. Multisystem inflammatory syndrome in children associated with severe acute respiratory syndrome coronavirus 2: a systematic review. *J Pediatr*. 2020;226:45–54.e1.
- 42 Del Rio C, Collins LF, Malani P. Long-term health consequences of COVID-19. *JAMA*. 2020;324(17):1723–1724.
- 43 Morris SB, Schwartz NG, Patel P, et al. Case series of multisystem inflammatory syndrome in adults associated with SARS-CoV-2 infection - United Kingdom and United States, March-August 2020. *MMWR Morb Mortal Wkly Rep*. 2020;69(40):1450–1456.
- 44 Ziegler CGK, Allon SJ, Nyquist SK, et al. SARS-CoV-2 receptor ACE2 is an interferon-stimulated gene in human airway epithelial cells and is detected in specific cell subsets across tissues. *Cell*. 2020;181(5):1016–1035.e19.
- 45 Loreni F, Mancino M, Biffo S. Translation factors and ribosomal proteins control tumor onset and progression: how? *Oncogene*. 2014;33(17):2145–2156.
- 46 Schwanhauser B, Busse D, Li N, et al. Global quantification of mammalian gene expression control. *Nature*. 2011;473(7347):337–342.
- 47 Zhou Z, Yang Z, Ou J, et al. Temperature dependence of the SARS-CoV-2 affinity to human ACE2 determines COVID-19 progression and clinical outcome. *Comput Struct Biotechnol J*. 2021;19:161–167.
- 48 Karlsson M, Zhang C, Mear L, et al. A single-cell type transcriptomics map of human tissues. *Sci Adv*. 2021;7(31).
- 49 De Caluwe L, Coppens S, Vereecken K, et al. The CD147 protein complex is involved in entry of chikungunya virus and related alphaviruses in human cells. *Front Microbiol*. 2021;12:615165.
- 50 Perez-Riverol Y, Bai J, Bandla C, et al. The PRIDE database resources in 2022: a hub for mass spectrometry-based proteomics evidences. *Nucleic Acids Res*. 2022;50(D1):D543–D552.